International Journal of Solids and Structures 113–114 (2017) 24–36

Contents lists available at ScienceDirect

International Journal of Solids and Structures

journal homepage: www.elsevier.com/locate/ijsolstr

Voltage-controlled complete stopbands in two-dimensional soft dielectrics

Roey Getz[a], Dennis M. Kochmann[b], Gal Shmuel[a,*]

[a] Faculty of Mechanical Engineering, Technion–Israel Institute of Technology, Haifa 32000, Israel
[b] Graduate Aerospace Laboratories, California Institute of Technology, Pasadena, CA 91125, USA

ARTICLE INFO

Article history:
Received 11 July 2016
Revised 21 September 2016
Available online 8 October 2016

Keywords:
Dielectric elastomer
Wave propagation
Band gap
Composite
Phononic crystal
Plane wave expansion
Nonlinear elasticity

ABSTRACT

Dielectric elastomers deform and stiffen when subjected to voltage. This work demonstrates how fiber composites made of incompressible dielectric elastomers exhibit *complete* band gaps—frequency ranges in which elastic wave propagation is prohibited, irrespective of its *polarization and direction*. To this end, we first analytically determine the quasi-static response of a wide class of composites to an electric field along the fibers. We then formulate and calculate incremental motions of general polarization propagating in the deformed composite, using a plane wave expansion approach. We numerically explore the dependency of the motion on the composite properties and electric field. We show how *complete* band gaps are tuned by adjusting the electric field, owing to resultant geometrical and physical changes. These results suggest that soft dielectrics can serve as tunable waveguides and filters.

1. Introduction

The frequency spectrum of periodic media exhibits bands, termed *band gaps* or *stopbands*, in which waves are forbidden from propagating. *Bragg* band gaps result from the multiple scattering and subsequent interference of incoming and refracted waves. When the periodic medium is elastic, this unusual phenomenon corresponds to the decay of mechanical motions (Kushwaha et al., 1993). Accordingly, elastic band gaps can be employed to suppress noise (Shen et al., 2015), isolate undesired vibrations (Olhoff et al., 2012), or conversely guide waves (Laude et al., 2005). To recall just a few of the relevant experiments, we refer to Garcia-Pablos et al. (2000); Vasseur et al. (2001); Wen et al. (2005); Schneider et al. (2012) and Celli and Gonella (2015).

Composites having tunable gaps are desirable since they can comply with changing needs at different frequencies. Prestress/strain is one approach to tune gaps (Bertoldi and Boyce, 2008; Feng and Liu, 2012; Huang et al., 2015; Barnwell et al., 2016); this mechanism, however, is difficult to accurately and actively control. An alternative approach considers composites made out of *smart* materials, whose physical properties are changed by application of external stimuli, *e.g.*, composites comprising shape-memory alloys (Ruzzene and Baz, 1999), piezoelectrics (Qian et al., 2008; Huang et al., 2014; Degraeve et al., 2015), and magneto-sensitive (Wang et al., 2009; Bayat and Gordaninejad, 2015) and dielectric elastomers (Gei et al., 2011; Shmuel and deBotton, 2012). The latter class attracts special interest, since dielectric elastomers are inexpensive, have low mass density, respond quickly, and reversibly undergo large deformations by application of voltage (Pelrine et al., 2000b; Cohen and deBotton, 2016). We consider fiber composites made out of these materials, and demonstrate the electrostatic tunability of the corresponding band structure. Specifically, we investigate incremental waves propagating on top of a finite deformation caused by application of voltage. Our idea is simple: as the electric field induces significant geometrical changes and modifies the constituent properties, the characteristics of the incremental motion and the resultant band gaps will change too. This is demonstrated in what follows, with the help of numerical examples based on analytical modeling.

As the sequel shows, we find *complete* gaps which are tunable by bias electric fields; by complete we mean gaps which are independent of the propagation direction *and* the plane of the motion. Thus, by calculating also displacements which are perpendicular to the fibers, *i.e.*, accounting for the in-plane motion, this work complements the findings of Shmuel (2013), who considered only displacements along the fibers, *i.e.*, considered only anti-plane waves. We note that Zhou and Chen (2013) have found electrostatically tunable in-plane gaps in a fiber composite consisting of a soft electrorheological phase; their model, however, uses linear elasticity, thereby not accounting for material and geometrical nonlinearities accompanying large deformations of elastomers. By

* Corresponding author.
E-mail address: meshmuel@tx.technion.ac.il (G. Shmuel).

http://dx.doi.org/10.1016/j.ijsolstr.2016.10.002
0020-7683/

contrast, using finite electroelasticity theory (Dorfmann and Ogden, 2005, 2010), we calculate the nonlinear deformation and subsequent motion of composites whose constituents are governed by a general class of nonlinear constitutive relations. By deriving a solution for this general class of material laws, we generalize the solution of Shmuel (2013), which was obtained for a specific model. The important question of electromechanical stability (Siboni and Castañeda, 2014; Siboni et al., 2014) is beyond the scope of this work, and to proceed we assume the deformation is in the stable regime. Subsequently, superposed motions are analyzed when using the Gent model (Gent, 1996). We note that the counterpart of the in-plane analysis for the uncoupled problem was never carried out, *i.e.*, for finitely deformed fiber composite comprising purely elastic incompressible phases, *a fortiori* for the coupled problem we address. We also note that in deriving forthcoming benchmark results, our idealized model neglects viscoelasticity. While this assumption is reasonable for silicones, viscoelasticity in acrylics is significantly more severe (Kornbluh and Pelrine, 2008).

The paper is organized as follows. Section 2 reviews the necessary theory to model motions of finitely deformed composites made out of soft dielectrics (Toupin, 1956; deBotton et al., 2007; Suo et al., 2008; Castañeda and Siboni, 2012; Liu, 2013; Lopez-Pamies, 2014). This theory is employed in Section 3 to analytically determine a voltage-induced deformation of a fiber composite whose phase behaviors are governed by general electroelastic laws. In Section 4 we formulate the equations governing incremental motions of general polarization propagating in the deformed plane. We develop a numerical generalized eigenvalue problem for a solution of the resultant equations, using a plane wave expansion approach (Kushwaha et al., 1993). Making use of numerical examples, Section 5 explores the band diagram of fiber composites whose mechanical response is Gentian (Gent, 1996). Specifically, we investigate the dependency of the diagram on the geometrical, electrical and mechanical properties, and—most significantly—the electric field. We summarize our main results and conclusions in Section 6.

2. Dynamics of electroelastic composites

Consider a deformable body composed of N homogeneous dielectric phases, and surrounded by vacuum. When no loads are applied, the body occupies the volume $\Omega_0 \subset \mathbb{R}^3$ in a reference configuration, and is bounded by $\partial\Omega_0$. By application of mechanical and/or electric loads, material points $\mathbf{X} \in \Omega_0$ at time t in the time interval $\mathscr{I} \in \mathbb{R}$, are mapped by a twice-differentiable deformation function $\boldsymbol{\chi} : \Omega_0 \times \mathscr{I} \to \mathbb{R}^3$, to their current position $\mathbf{x} = \boldsymbol{\chi}(\mathbf{X}, t)$. Thereby, the current configuration of the body Ω and current boundary $\partial\Omega$ are defined. The gradient of the deformation is denoted by $\mathbf{F} = \nabla_{\mathbf{X}}\boldsymbol{\chi} := \partial\boldsymbol{\chi}/\partial\mathbf{X}$. Line, area and volume elements in the neighborhood of $\mathbf{X}$ are denoted with $\mathrm{d}\mathbf{X}$, $\mathrm{d}A$, and $\mathrm{d}V$, respectively. These are mapped to their counterparts in the current configuration $\mathrm{d}\mathbf{x}$, $\mathrm{d}a$ and $\mathrm{d}v$ according to $\mathrm{d}\mathbf{x} = \mathbf{F}\mathrm{d}\mathbf{X}$, $\mathbf{n}\mathrm{d}a = J\mathbf{F}^{-\mathrm{T}}\mathbf{N}\mathrm{d}A$ and $\mathrm{d}v = J\mathrm{d}V$, where $J \equiv \det\mathbf{F} > 0$, and $\mathbf{N}$ and $\mathbf{n}$ are unit normals of referential and deformed area elements, respectively. The compositions $\mathbf{C} = \mathbf{F}^{\mathrm{T}}\mathbf{F}$, $\mathbf{b} = \mathbf{F}\mathbf{F}^{\mathrm{T}}$ are termed the right and left Cauchy-Green strain tensors, respectively, and serve as strain measures.

The presence of charge in the current configuration is accompanied by an electric field $\mathbf{e}$ and an electric displacement field $\mathbf{d}$. The constitutive behavior of the body dictates the relation between the fields; in vacuum they are linearly related via the permittivity ϵ_0. Maxwell equations governing these fields read

$$\nabla \cdot \mathbf{d} = 0, \ \nabla \times \mathbf{e} = \mathbf{0}, \tag{1}$$

where $\nabla\cdot(\bullet)$ and $\nabla\times(\bullet)$ are the divergence and curl operators, respectively, evaluated in Ω with respect to $\mathbf{x}$. The form of the first of Eq. (1) is due to the absence of body charge in dielectrics. The second of Eq. (1) tacitly uses an electrostatic approximation, appropriate when at the considered frequencies, the length of the mechanical waves is significantly shorter than its electromagnetic counterpart.

Accounting for coupling between elastic and electric interactions, the balance of linear momentum in terms of the *total* stress tensor $\boldsymbol{\sigma}$ is (Dorfmann and Ogden, 2005)

$$\nabla \cdot \boldsymbol{\sigma} = \rho\boldsymbol{\chi}_{,tt}, \tag{2}$$

ρ being the current mass density.

Jump conditions across boundaries between adjacent phases m and f free of charge are written as

$$[\![\boldsymbol{\sigma}]\!]\mathbf{n} = \mathbf{0}, \quad [\![\mathbf{d}]\!]\cdot\mathbf{n} = 0, \quad [\![\mathbf{e}]\!]\times\mathbf{n} = \mathbf{0}, \tag{3}$$

where $[\![\bullet]\!] \equiv (\bullet)^{(m)} - (\bullet)^{(f)}$; herein and henceforth $(\bullet)^{(p)}$ denotes the value of $(\bullet)$ in phase p. Jump conditions at the outer boundary between the body and the vacuum read

$$(\boldsymbol{\sigma} - \boldsymbol{\sigma}^\star)\mathbf{n} = \mathbf{t}_m, \quad (\mathbf{d} - \mathbf{d}^\star)\cdot\mathbf{n} = -w_e, \quad (\mathbf{e} - \mathbf{e}^\star)\times\mathbf{n} = \mathbf{0}, \tag{4}$$

where $\mathbf{t}_m$ is a prescribed mechanical traction, w_e is a surface charge density, and $(\bullet)^\star$ denotes fields in vacuum. Specifically, $\boldsymbol{\sigma}^\star$ is known as the Maxwell stress, given by

$$\boldsymbol{\sigma}^\star = \epsilon_0\left[\mathbf{e}^\star\otimes\mathbf{e}^\star - \frac{1}{2}(\mathbf{e}^\star\cdot\mathbf{e}^\star)\mathbf{I}\right]. \tag{5}$$

A Lagrangian formulation uses the following *pull-backs* of the governing fields

$$\mathbf{P} = J\boldsymbol{\sigma}\mathbf{F}^{-\mathrm{T}}, \quad \mathbf{D} = J\mathbf{F}^{-1}\mathbf{d}, \quad \mathbf{E} = \mathbf{F}^{\mathrm{T}}\mathbf{e}. \tag{6}$$

We refer to **P, D**, and **E** as the *total* first Piola-Kirchhoff stress, Lagrangian electric displacement, and Lagrangian electric field, respectively. These satisfy a Lagrangian form of the governing Eqs. (2) in Ω_0, namely,

$$\nabla_{\mathbf{X}}\cdot\mathbf{P} = \rho_L\boldsymbol{\chi}_{,tt}, \quad \nabla_{\mathbf{X}}\cdot\mathbf{D} = 0, \quad \nabla_{\mathbf{X}}\times\mathbf{E} = \mathbf{0}, \tag{7}$$

where $\rho_L = J\rho$. Lagrangian counterparts of Eqs. (3) and (4) are

$$(\mathbf{P} - \mathbf{P}^\star)\mathbf{N} = \mathbf{t}_M, \quad (\mathbf{D} - \mathbf{D}^\star)\cdot\mathbf{N} = -w_E, \quad (\mathbf{E} - \mathbf{E}^\star)\times\mathbf{N} = \mathbf{0}, \tag{8}$$

$$[\![\mathbf{P}]\!]\mathbf{N} = \mathbf{0}, \quad [\![\mathbf{D}]\!]\cdot\mathbf{N} = 0, \quad [\![\mathbf{E}]\!]\times\mathbf{N} = \mathbf{0}. \tag{9}$$

where $\mathbf{t}_M\mathrm{d}A = \mathbf{t}_m\mathrm{d}a$ and $w_E\mathrm{d}A = w_e\mathrm{d}a$.

An augmented energy density function $\Psi(\mathbf{F}, \mathbf{D}, \mathbf{X})$ determines **P** and **E** according to (Dorfmann and Ogden, 2005)

$$\mathbf{P} = \frac{\partial\Psi}{\partial\mathbf{F}}, \quad \mathbf{E} = \frac{\partial\Psi}{\partial\mathbf{D}}. \tag{10}$$

If the material is incompressible, the first of Eq. (10) is replaced with

$$\mathbf{P} = \frac{\partial\Psi}{\partial\mathbf{F}} - p_0\mathbf{F}^{-\mathrm{T}}, \tag{11}$$

where p_0 is a Lagrangian multiplier accounting for the kinematic constraint $\det\mathbf{F} = 1$.

Let the pair $\boldsymbol{\chi}$ and **D** satisfy the static boundary-value problem. The formulation of the equations governing superposed incremental motions rests on small time-dependent elastic and electric displacements, denoted $\dot{\boldsymbol{\chi}}(\mathbf{X}, t)$ and $\dot{\mathbf{D}}(\mathbf{X}, t)$, respectively. Herein and in the sequel, we use superposed dots to denote increments. Linear approximations of Eq. (10) derived using Taylor series are

$$\dot{\mathbf{P}} = \mathscr{C}_0\dot{\mathbf{F}} + p_0\mathbf{F}^{-\mathrm{T}}\dot{\mathbf{F}}^{\mathrm{T}}\mathbf{F}^{-\mathrm{T}} - \dot{p}_0\mathbf{F}^{-\mathrm{T}} + \mathscr{B}_0\dot{\mathbf{D}}, \quad \dot{\mathbf{E}} = \mathscr{B}_0^{\mathrm{T}}\dot{\mathbf{F}} + \mathscr{A}_0\dot{\mathbf{D}}, \tag{12}$$

where $\left(\mathscr{B}_0^{\mathrm{T}}\dot{\mathbf{F}}\right)_k = \mathscr{B}_{0ijk}\dot{F}_{ij}$, $\dot{\mathbf{F}} = \nabla_{\mathbf{X}}\dot{\boldsymbol{\chi}}$. The tensors $\mathscr{A}_0$, $\mathscr{B}_0$ and $\mathscr{C}_0$ are defined by the components

$$\mathscr{A}_{0\alpha\beta} = \frac{\partial^2\Psi}{\partial D_\alpha\partial D_\beta}, \quad \mathscr{B}_{0i\alpha\beta} = \frac{\partial^2\Psi}{\partial F_{i\alpha}\partial D_\beta}, \quad \mathscr{C}_{0i\alpha k\beta} = \frac{\partial^2\Psi}{\partial F_{i\alpha}\partial F_{k\beta}}. \tag{13}$$

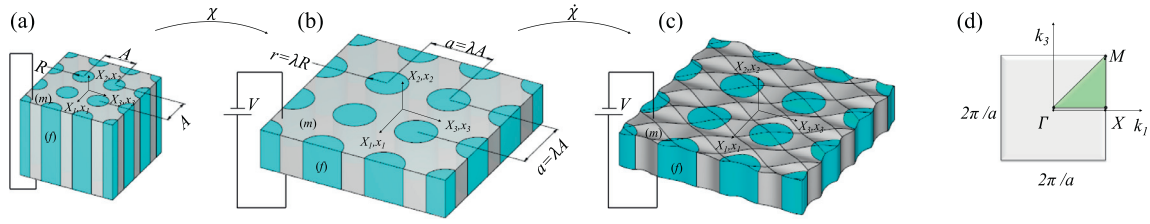

Fig. 1. Fiber composite made of dielectric elastomers (a) in the reference configuration; (b) in the deformed configuration, subjected to an electric field in the fiber direction; (c) when incremental motions are superposed. (d) Corresponding first irreducible Brillouin zone in the reciprocal space.

We can use the deformed configuration as an updated reference configuration. To this end, we *push-forward* the linear approximations, and define

$$\mathbf{\Sigma} = J^{-1}\dot{\mathbf{P}}\mathbf{F}^{\mathrm{T}}, \quad \check{\mathbf{d}} = J^{-1}\mathbf{F}\dot{\mathbf{D}}, \quad \check{\mathbf{e}} = \mathbf{F}^{-\mathrm{T}}\dot{\mathbf{E}}. \tag{14}$$

The updated versions satisfy

$$\nabla\cdot\mathbf{\Sigma} = \rho\dot{\mathbf{x}}_{,tt}, \quad \nabla\cdot\check{\mathbf{d}} = 0, \quad \nabla\times\check{\mathbf{e}} = \mathbf{0}, \tag{15}$$

where $\dot{\mathbf{x}}(\mathbf{x},t) := \dot{\boldsymbol{\chi}}(\mathbf{X},t)$. In terms of the latter, the incremental incompressibility constraint is

$$\mathrm{tr}\mathbf{h} = 0, \tag{16}$$

where $\mathbf{h} = \nabla\dot{\mathbf{x}}$. Rewriting Eq. (12) with updated quantities provides the compact form

$$\mathbf{\Sigma} = \mathscr{C}\mathbf{h} + p_0\mathbf{h}^{\mathrm{T}} - \dot{p}_0\mathbf{I} + \mathscr{B}\check{\mathbf{d}}, \quad \check{\mathbf{e}} = \mathscr{B}^{\mathrm{T}}\mathbf{h} + \mathscr{A}\check{\mathbf{d}}, \tag{17}$$

with

$$\mathscr{A}_{ij} = JF^{-1}_{\alpha i}\mathscr{A}_{0\alpha\beta}F^{-1}_{\beta j}, \quad \mathscr{B}_{ijk} = F_{j\alpha}\mathscr{B}_{0i\alpha\beta}F^{-1}_{\beta k}, \quad \mathscr{C}_{ijkl} = J^{-1}F_{j\alpha}\mathscr{C}_{0i\alpha k\beta}F_{l\beta}. \tag{18}$$

3. Soft dielectric fiber composites under an axial electric field

Determining the exact response of a soft dielectric is a difficult task, on account of the corresponding coupled nonlinear equations. These nonlinear coupled equations stem from the geometrical nonlinearity, material nonlinearity, and the coupling between the electrical and mechanical fields. Nevertheless, we show that the following problem belongs to a class of problems which can be solved exactly, independently of the specific form of the material constitutive behavior. A catalog of such problems for *homogeneous* soft dielectrics was given by Singh and Pipkin (1966), when the deformation and the electric field are postulated at the outset (see also Bustamante and Ogden, 2006). We provide a solution for the problem of a fiber *composite* comprising transversely isotropic phases. The fibers are aligned along the preferred direction, but otherwise their geometry is arbitrary. The solution rests on the establishment of piecewise uniform fields by proper boundary conditions (see Benveniste and Dvorak, 1992, in the piezoelectric counterpart). A complete description of the problem and its solution is provided next.

Consider an incompressible composite made out of deformable dielectric fibers (phase f) embedded periodically in a different soft dielectric matrix (phase m). We assume that the fibers are infinitely long, and treat the composite as two-dimensional whose corresponding fields are invariant with respect to the axial direction. We restrict attention to constituents whose material symmetry is initially transversely isotropic about the direction of the fibers. In the reference configuration, the distance between centers of adjacent fibers is A (Fig. 1a). The composite is coated with stretchable electrodes at the far upper and lower surfaces perpendicular to the fibers. By creating a voltage difference V between the electrodes, an electric field $\mathbf{e}$ evolves in the fibers direction. The outstanding issue is to determine the resultant deformation and stress brought by the electric field.

Before proceeding to the solution, we note that the placement we address for the electrodes is different from the typical placement considered, *i.e.*, in parallel to the direction of the fibers (Lu et al., 2012; Siboni and Castañeda, 2014; Lefèvre and Lopez-Pamies, 2015). The motivation for the configuration we describe is to use the fibers as scatterers for elastic waves propagating in the periodicity plane. A realization of such in-plane arrangement of phases is promoted by the rapid development of 3D printing technology. A review on this topic by Raney and Lewis (2015) states that *"3D printing of nearly arbitrary, 3D mesoscale architectures can be printed with minimum feature sizes ranging from ∼ 100 nm to 100 μm from multiple classes of materials"*. In particular, we refer to Creegan and Anderson (2014), who demonstrated a proof of concept of dielectric elastomer 3D printing in two materials using stereolithography.

Proceeding with the solution derivation, we begin by postulating a piecewise-homogeneous deformation. In a Cartesian coordinate system in which x_2 is along the fibers and (x_1, x_3) is the periodicity plane (Fig. 1b), the matrix representation of $\mathbf{F}$ in each phase is

$$\mathsf{F}^{(p)} = \mathrm{diag}\left[\lambda_1^{(p)}, \left(\lambda_1^{(p)}\lambda_3^{(p)}\right)^{-1}, \lambda_3^{(p)}\right]. \tag{19}$$

By virtue of the transverse isotropy of the phases, $\mathsf{F}^{(p)}$ is diagonal in the coordinates employed. Further note that $\mathsf{F}^{(p)}$ is compatible with the requirement $\det\mathbf{F}^{(p)} = 1$. Assuming perfect bonding between the phases, the stretch ratios in the fiber direction must be the same, therefore

$$\left(\lambda_1^{(m)}\lambda_3^{(m)}\right)^{-1} = \left(\lambda_1^{(f)}\lambda_3^{(f)}\right)^{-1}. \tag{20}$$

On account of symmetry in the geometry and boundary conditions with respect to the (x_1, x_3) plane, the in-plane stretches of each phase are equal, *i.e.*,

$$\lambda_1^{(p)} = \lambda_3^{(p)}. \tag{21}$$

Eqs. (20) and (21) reveal that the overall deformation is homogeneous, such that

$$\mathsf{F}^{(m)} = \mathsf{F}^{(f)} = \mathrm{diag}\,[\lambda, \lambda^{-2}, \lambda]. \tag{22}$$

To proceed with calculating λ, the energy density for each phase is required; we assume these are of the form

$$\Psi^{(p)} = W^{(p)}(I_1) + \frac{1}{2\epsilon^{(p)}}\left(\gamma_0^{(p)}I_{4e} + \gamma_1^{(p)}I_{5e} + \gamma_2^{(p)}I_{6e}\right), \tag{23}$$

where $I_1 = \mathrm{tr}\mathbf{C}$, $I_{4e} = \mathbf{D}\cdot\mathbf{D}$, $I_{5e} = \mathbf{D}\cdot\mathbf{C}\mathbf{D}$, and $I_{6e} = \mathbf{D}\cdot\mathbf{C}^2\mathbf{D}$. Eq. (23) states that the material response depends (perhaps nonlinearly) on I_1 through $W^{(p)}(I_1)$, and linearly on I_{4e}, I_{5e} and I_{6e} through $\gamma_0^{(p)}/\epsilon^{(p)}$, $\gamma_1^{(p)}/\epsilon^{(p)}$ and $\gamma_2^{(p)}/\epsilon^{(p)}$, respectively. The general form of the energy (23) agrees with the common approach to model soft dielectrics, namely, augmenting a purely mechanical part that captures the behavior of elastomers and depends on I_1, with a part that accounts for the electromechanical coupling in finite deformations. Popular models in rubber elasticity that

belong to the class described by $W(I_1)$ are the Arruda–Boyce model (Arruda and Boyce, 1993), the Gent model (Gent, 1996), and of course the neo-Hookean model.[1] The augmented part in Eq. (23) captures dielectrics whose permittivity varies with strain (Cohen et al., 2016), and which have been referred to as electrostrictive (Zhao and Suo, 2008). The specific augmented form in Eq. (23) was employed, *e.g.*, by Dorfmann and Ogden (2005) and Gei et al. (2014). By constraining $\sum_i \gamma_i^{(p)} = 1$, we obtain the linear relation $\mathbf{d}^{(p)} = \epsilon^{(p)}\mathbf{e}^{(p)}$ when there is no deformation; we identify $\epsilon^{(p)}$ with the dielectric constant, such that $\epsilon^{(p)} = \epsilon_r^{(p)}\epsilon_0$, and $\epsilon_r^{(p)}$ is the relative dielectric constant of phase p.

Applying Eq. (11) to the deformation (22) and the energies (23) provides the non-vanishing stress components

$$\sigma_{11}^{(p)} = \sigma_{33}^{(p)} = \check{\mu}^{(p)}\lambda^2 - p_0^{(p)}, \tag{24a}$$

$$\sigma_{22}^{(p)} = \check{\mu}^{(p)}\lambda^{-4} + \epsilon^{(p)}\xi^{(p)}e_2^{(p)^2} - p_0^{(p)}, \tag{24b}$$

where $\check{\mu}^{(p)} = 2\frac{\partial W^{(p)}}{\partial I_1}$ and $\xi^{(p)} = \frac{\lambda^8\gamma_1^{(p)}+2\lambda^4\gamma_2^{(p)}}{(\lambda^8\gamma_0^{(p)}+\lambda^4\gamma_1^{(p)}+\gamma_2^{(p)})^2}$. At interfaces between the phases in the (x_1, x_3)-plane, the last of Eq. (3) is satisfied with

$$e_2^{(m)} = e_2^{(f)} = e_2. \tag{25}$$

Note that the solution in (25) holds for any unit normal in the (x_1, x_3) plane, and therefore it is valid for any geometry of fibers parallel to the x_2-axis. Application of relation (10) to the model (23) with the deformation (22) delivers the following resultant electric displacement field in each phase

$$d_2^{(p)} = \left(\lambda^4\gamma_0^{(p)} + \gamma_1^{(p)} + \lambda^{-4}\gamma_2^{(p)}\right)^{-1}\epsilon^{(p)}e_2. \tag{26}$$

Since the electric displacement field in each phase is in the x_2-direction, the second of Eq. (3) is satisfied for any in-plane unit normal, and hence applies for any microstructure of unidirectional fibers.

Traction continuity across the interfaces, together with an expansion-free boundary condition in the (x_1, x_3) plane implies

$$\sigma_{11}^{(p)} = \sigma_{33}^{(p)} = 0. \tag{27}$$

We recall that the diagonal deformation creates a triaxial state of stress in the transversely isotropic phases, *i.e.*, $\sigma_{13}^{(p)} = \sigma_{31}^{(p)} = 0$. Accordingly, satisfying Eq. (27) guarantees traction continuity at interfaces defined by any unit normal in the (x_1, x_3) plane, and hence the first of Eq. (3) is guaranteed independently of the shape of the fiber cross-section. The Lagrangian multiplier calculated through Eq. (27) is

$$p_0^{(p)} = \check{\mu}^{(p)}\lambda^2. \tag{28}$$

The solution is completed by satisfying the condition associated with the absence of mechanical forces at the electrodes, namely

$$\bar{\sigma}_{22} = 0, \tag{29}$$

where $(\bar{\bullet}) = v^{(f)}(\bullet)^{(f)} + v^{(m)}(\bullet)^{(m)}$, and $v^{(f)}$ and $v^{(m)} = 1 - v^{(f)}$ are the volume fractions of the fiber and matrix phases, respectively. Upon substitution of Eq. (28) into Eq. (29), in conjunction with Eq. (24b), we find the relation between the in-plane stretch ratio λ and the current electric field e_2, namely

$$\overline{\left(\frac{\check{\mu}(I_1)}{\xi(\lambda)}\right)}\left(\lambda^2 - \lambda^{-4}\right) = \bar{\epsilon}e_2^2. \tag{30}$$

Relation (30) generalizes a result by Shmuel (2013) to composites whose dependency on I_1 is general, and whose permittivity depends on the deformation.

[1] For a discussion on the invariants in electroelasticity and anisotropic elasticity see Bustamante and Shariff (2016), Shariff (2011) and the references therein.

Before we proceed to analyze superposed motions, we emphasize that the determined homogeneous deformation is an *exact solution* for the considered problem, as its corresponding fields satisfy the governing equations and boundary conditions. Essentially, we arrived at the counterpart of the result of Benveniste and Dvorak (1992) in the piezoelectric case, therein *"the existence of uniform fields which can be generated by the application of certain mechanical and electrical boundary conditions in such composites is established"*.

4. Elastic waves in actuated soft dielectric fiber composites

We are interested in characterizing *general* superposed motions propagating in the (x_1, x_3) plane of the deformed composite (Fig. 1c); by general we mean that both the in-plane ($\dot{x}_1$ and $\dot{x}_3$) and the anti-plane ($\dot{x}_2$) components of the incremental displacement field do not vanish. By contrast, Shmuel (2013) considered only an anti-plane motion, thereby assumed that $\dot{x}_1$ and $\dot{x}_3$ are zero.

We begin by examining the resultant incompressibility constraint (16), which reads

$$\dot{x}_{1,1} + \dot{x}_{3,3} = 0. \tag{31}$$

Therefore, the in-plane components can be derived from a stream function $\phi(x_1, x_3, t)$, such that

$$\dot{x}_1 = \phi_{,3}, \quad \dot{x}_3 = -\phi_{,1}. \tag{32}$$

The last of Eq. (15) implies that $\check{\mathbf{e}}$ can also be derived from a scalar potential, say $\varphi(x_1x_3, t)$, via

$$\check{\mathbf{e}} = -\nabla\varphi. \tag{33}$$

In terms of the unknowns ϕ, $\dot{x}_2$ and φ, the incremental governing Eqs. (15) are

$$\rho^{(p)}(\mathbf{x})\phi_{,3tt} = 2(\hat{\mu}^{(p)}(\mathbf{x})\phi_{,13})_{,1} + (\hat{\mu}^{(p)}(\mathbf{x})\phi_{,33})_{,3} - (\hat{\mu}^{(p)}(\mathbf{x})\phi_{,11})_{,3} - \dot{p}_{0,1}(\mathbf{x}, t), \tag{34a}$$

$$\rho^{(p)}(\mathbf{x})\phi_{,1tt} = 2\left(\hat{\mu}^{(p)}(\mathbf{x})\phi_{,13}\right)_{,3} + \left(\hat{\mu}^{(p)}(\mathbf{x})\phi_{,11}\right)_{,1} - (\hat{\mu}^{(p)}(\mathbf{x})\phi_{,33})_{,1} + \dot{p}_{0,3}(\mathbf{x}, t), \tag{34b}$$

$$\rho^{(p)}(\mathbf{x})\dot{x}_{2,tt} = \nabla_T \cdot \left(\tilde{\mu}^{(p)}(\mathbf{x})\nabla_T\dot{x}_2 - \tilde{d}_2^{\,(p)}(\mathbf{x})\nabla_T\varphi\right), \tag{34c}$$

$$0 = \nabla_T \cdot \left(-\tilde{d}_2^{\,(p)}(\mathbf{x})\nabla_T\dot{x}_2 - \tilde{\epsilon}^{(p)}(\mathbf{x})\nabla_T\varphi\right), \tag{34d}$$

where $\nabla_T(\bullet) = \mathbf{i}_1(\bullet)_{,1} + \mathbf{i}_3(\bullet)_{,3}$ is the in-plane gradient operator, $\mathbf{i}_1$ and $\mathbf{i}_3$ are unit vectors in the x_1 and x_3 directions, respectively; the quantities $\hat{\mu}^{(p)}(\mathbf{x})$, $\tilde{\mu}^{(p)}(\mathbf{x})$, $\tilde{d}_2^{\,(p)}(\mathbf{x})$ and $\tilde{\epsilon}^{(p)}(\mathbf{x})$ are listed in Appendix B, and were derived using a specialization of the constitutive tensors given in Appendix A. Interestingly, Eqs. (34a) and (34b) decouple from Eqs. (34c) and (34d), however they are coupled with one another. Accordingly, the in-plane mode decouples from the anti-plane mode and from the incremental electric field.

To determine ϕ, Eqs. (34a) and (34b) are cross-differentiated and summed to obtain

$$\nabla_T \cdot \left(\rho^{(p)}(\mathbf{x})\nabla_T\phi_{,tt}\right) = 4\left(\hat{\mu}^{(p)}(\mathbf{x})\phi_{,13}\right)_{,13} + \left(\hat{\mu}^{(p)}(\mathbf{x})\phi_{,11}\right)_{,11} + \left(\hat{\mu}^{(p)}(\mathbf{x})\phi_{,33}\right)_{,33} - \left(\hat{\mu}^{(p)}(\mathbf{x})\phi_{,11}\right)_{,33} - \left(\hat{\mu}^{(p)}(\mathbf{x})\phi_{,33}\right)_{,11}. \tag{35}$$

Eqs. (34c), (34d) and (35) are solved with a plane wave expansion approach (Kushwaha et al., 1993). We first expand $\hat{\mu}$, $\tilde{\mu}$, ρ,

$\tilde{\epsilon}$ and $\tilde{d}_2$ in two-dimensional Fourier series on account of their in-plane periodicity, and write

$$\zeta(\mathbf{x}) = \sum_{\mathbf{G}} \zeta(\mathbf{G}) \exp(i\mathbf{G}\cdot\mathbf{x}), \quad \zeta = \hat{\mu}, \tilde{\mu}, \rho, \tilde{\epsilon}, \tilde{d}_2, \tag{36}$$

$\{\zeta(\mathbf{G})\}$ being the Fourier coefficients associated with the infinite set of reciprocal lattice vectors $\{\mathbf{G}\}$. The Bravais lattice of the deformed composite is based on a square unit cell of period $a = \lambda A$. The reciprocal lattice is of square-type too, and therefore $\{\mathbf{G}|\mathbf{G} = \frac{2\pi}{a}(n_1\mathbf{i}_1 + n_3\mathbf{i}_3); n_1, n_3 \in \mathbb{N}\}$. Inverting the Fourier transform provides

$$\zeta(\mathbf{G}) = \begin{cases} \zeta^{(f)}\nu^{(f)} + \zeta^{(m)}(1-\nu^{(f)}) \equiv \bar{\zeta} & \mathbf{G} = \mathbf{0}, \\ (\zeta^{(f)} - \zeta^{(m)})S(\mathbf{G}) \equiv \Delta\zeta S(\mathbf{G}) & \mathbf{G} \neq \mathbf{0}, \end{cases} \tag{37}$$

where $S(\mathbf{G}) = \frac{1}{a^2}\iint_{a^{(f)}} \exp(-i\mathbf{G}\cdot\mathbf{x})\mathrm{d}a$, and $a^{(f)}$ is the cross-sectional area of the fiber phase.

Next, by virtue of the Bloch theorem (Kittel, 2005), we expand the incremental fields ϕ, $\dot{x}_2$ and φ in the form

$$\vartheta(\mathbf{x}, t) = \sum_{\mathbf{G}'} \vartheta(\mathbf{G}') \exp[i(\mathbf{G}'+\mathbf{k})\cdot\mathbf{x} - i\omega t], \quad \vartheta = \phi, \dot{x}_2, \varphi, \tag{38}$$

where ω is the angular frequency, $\mathbf{k} = k_1\mathbf{i}_1 + k_3\mathbf{i}_3$ is the two-dimensional Bloch wave vector, and the summation is carried over the reciprocal lattice vectors. Expansions (37) and (38) are inserted into Eqs. (34c), (34d) and (35), yielding

$$\begin{aligned} &\Big\{\sum_{\mathbf{G},\mathbf{G}'}[\tilde{\mu}(\mathbf{G}-\mathbf{G}')\dot{x}_2(\mathbf{G}') - \tilde{d}_2(\mathbf{G}-\mathbf{G}')\varphi(\mathbf{G}')](\mathbf{G}'+\mathbf{k})\cdot(\mathbf{G}+\mathbf{G}'+\mathbf{k}) \\ &\times \exp[i(\mathbf{G}+\mathbf{G}')\cdot\mathbf{x} - i\omega t] - \omega^2\rho(\mathbf{G}-\mathbf{G}')\dot{x}_2(\mathbf{G}') \\ &\times \exp[i(\mathbf{G}+\mathbf{G}')\cdot\mathbf{x} - i\omega t]\Big\}\exp(i\mathbf{k}\cdot\mathbf{x}) = 0, \end{aligned} \tag{39a}$$

$$\begin{aligned} &\Big\{\sum_{\mathbf{G},\mathbf{G}'}[-\tilde{d}_2(\mathbf{G}-\mathbf{G}')\dot{x}_2(\mathbf{G}') - \tilde{\epsilon}(\mathbf{G}-\mathbf{G}')\varphi(\mathbf{G}')] \times (\mathbf{G}'+\mathbf{k}) \\ &\cdot (\mathbf{G}+\mathbf{G}'+\mathbf{k})\exp[i(\mathbf{G}+\mathbf{G}')\cdot\mathbf{x} - i\omega t]\Big\}\exp(i\mathbf{k}\cdot\mathbf{x}) = 0, \end{aligned} \tag{39b}$$

$$\begin{aligned} &\Big\{\sum_{\mathbf{G},\mathbf{G}'}\hat{\mu}(\mathbf{G}-\mathbf{G}')\phi(\mathbf{G}') \\ &\times \Big\{4(\mathbf{G}'+\mathbf{k})_1(\mathbf{G}'+\mathbf{k})_3(\mathbf{G}+\mathbf{G}'+\mathbf{k})_1(\mathbf{G}+\mathbf{G}'+\mathbf{k})_3 \\ &+ \Big[(\mathbf{G}'+\mathbf{k})_1^2 - (\mathbf{G}'+\mathbf{k})_3^2\Big]\Big[(\mathbf{G}+\mathbf{G}'+\mathbf{k})_1^2 - (\mathbf{G}+\mathbf{G}'+\mathbf{k})_3^2\Big]\Big\} \\ &\times \exp[i(\mathbf{G}+\mathbf{G}')\cdot\mathbf{x} - i\omega t] - \omega^2\rho(\mathbf{G}-\mathbf{G}')\phi(\mathbf{G}')(\mathbf{G}'+\mathbf{k}) \\ &\cdot (\mathbf{G}+\mathbf{G}'+\mathbf{k})\exp[i(\mathbf{G}+\mathbf{G}')\cdot\mathbf{x} - i\omega t]\Big\}\exp(i\mathbf{k}\cdot\mathbf{x}) = 0. \end{aligned} \tag{40}$$

Since the above equations hold for any $\mathbf{x}$, the sums in the curly brackets must vanish. We then multiply these sums by $\exp(-i\mathbf{G}''\cdot\mathbf{x})$ and integrate the result over the unit-cell. The orthogonality of the Fourier functions implies that only terms for which $\mathbf{G}'' = \mathbf{G}+\mathbf{G}'$ remain in the summation. Thus, the final set of equations is

$$\begin{aligned} &\sum_{\mathbf{G}'}(\tilde{\mu}(\mathbf{G}-\mathbf{G}')\dot{x}_2(\mathbf{G}') - \tilde{d}_2(\mathbf{G}-\mathbf{G}')\varphi(\mathbf{G}'))(\mathbf{G}'+\mathbf{k})\cdot(\mathbf{G}+\mathbf{k}) \\ &= \omega^2\sum_{\mathbf{G}'}\rho(\mathbf{G}-\mathbf{G}')\dot{x}_2(\mathbf{G}'), \end{aligned} \tag{41a}$$

$$\sum_{\mathbf{G}'}(-\tilde{d}_2(\mathbf{G}-\mathbf{G}')\dot{x}_2(\mathbf{G}') - \tilde{\epsilon}(\mathbf{G}-\mathbf{G}')\varphi(\mathbf{G}'))(\mathbf{G}'+\mathbf{k})\cdot(\mathbf{G}+\mathbf{k}) = 0, \tag{41b}$$

$$\begin{aligned} &\sum_{\mathbf{G}'}\hat{\mu}(\mathbf{G}-\mathbf{G}')\phi(\mathbf{G}')\Big\{4(\mathbf{G}'+\mathbf{k})_1(\mathbf{G}'+\mathbf{k})_3(\mathbf{G}+\mathbf{k})_1(\mathbf{G}+\mathbf{k})_3 \\ &+ \Big[(\mathbf{G}'+\mathbf{k})_1^2 - (\mathbf{G}'+\mathbf{k})_3^2\Big]\Big[(\mathbf{G}+\mathbf{k})_1^2 - (\mathbf{G}+\mathbf{k})_3^2\Big]\Big\} \\ &= \omega^2\sum_{\mathbf{G}'}\rho(\mathbf{G}-\mathbf{G}')\phi(\mathbf{G}')(\mathbf{G}'+\mathbf{k})\cdot(\mathbf{G}+\mathbf{k}). \end{aligned} \tag{42}$$

Eqs. (41) and (42) are concisely written in matrix form as follows

$$\begin{pmatrix} Q^{(1,1)} & Q^{(1,2)} \\ Q^{(2,1)} & Q^{(2,2)} \end{pmatrix}\begin{bmatrix} \dot{x}_2(\mathbf{G}') \\ \varphi(\mathbf{G}') \end{bmatrix} = \omega^2\begin{pmatrix} R^{(1,1)} & 0 \\ 0 & 0 \end{pmatrix}\begin{bmatrix} \dot{x}_2(\mathbf{G}') \\ 0 \end{bmatrix}, \tag{43}$$

$$Q\phi(\mathbf{G}') = \omega^2 R\phi(\mathbf{G}'); \tag{44}$$

the components of Q, R, $Q^{(1,1)}$, $Q^{(1,2)}$, $Q^{(2,1)}$, $Q^{(2,2)}$ and $R^{(1,1)}$ are given in Appendix C. Eq. (43) implies that

$$\varphi(\mathbf{G}') = -Q^{(2,2)^{-1}}Q^{(2,1)}\dot{x}_2(\mathbf{G}'). \tag{45}$$

We substitute Eq. (45) back into Eq. (43) and obtain

$$\tilde{Q}\dot{x}_2(\mathbf{G}') = \omega^2 R^{(1,1)}\dot{x}_2(\mathbf{G}'), \tag{46}$$

where

$$\tilde{Q} = Q^{(1,1)} - Q^{(1,2)}Q^{(2,2)^{-1}}Q^{(2,1)}. \tag{47}$$

Eqs. (44) and (46) constitute a generalized eigenvalue problem for the eigenfrequencies ω, at a given wave vector $\mathbf{k}$. It is sufficient to consider only wave vectors within the irreducible first Brillouin zone, which defines the smallest region of unique wave propagation (Kittel, 2005). For a square lattice, the periphery of the zone is defined by the lines connecting the points $\Gamma = (0,0)$, $X = (\pi/a, 0)$ and $M = (\pi/a, \pi/a)$, as illustrated in Fig. 1d. Under certain conditions, one can restrict attention to that periphery to determine the gap boundaries, since there the gaps almost always attain their extrema (Harrison et al., 2007; Craster et al., 2012). This was found to be true in similar problems, by scanning the interior of the zone (Kushwaha et al., 1994; Vasseur et al., 1994).

A numerical realization requires a truncation of the infinite-dimensional systems (44) and (46), by using a finite subset of $\{\mathbf{G}\}$. In the following, we have found that 441 plane waves, corresponding to $10 \leq n_1, n_3 \leq 10$, are sufficient for convergence. The numerical scheme and forthcoming results were implemented using Wolfram Mathematica 10.

5. Numerical investigation

With the help of numerical examples, we explore the band structure dependency on the properties of the composite and on the bias electric field. We consider circular fibers; the resultant structure function is $S(\mathbf{G}) = 2\frac{\pi R^2}{A^2}\frac{J_1(G\lambda R)}{G\lambda R}$, where R is the referential fiber radius, and J_1 is the Bessel function of the first kind of order 1. We use the Dielectric Gent energy (DG)

$$\Psi_{DG}^{(p)} = -\frac{\mu^{(p)}J_m^{(p)}}{2}\ln\left(1 - \frac{I_1 - 3}{J_m^{(p)}}\right) + \frac{1}{2\epsilon^{(p)}}I_{5e} \tag{48}$$

to model the constitutive behavior of each phase; $\mu^{(p)}$ correlates with the shear modulus in linear elasticity, where the constant $J_m^{(p)}$ models the elastomeric stiffening near a limiting strain (Gent, 1996). This *lock-up* effect results from the finite extensibility of the polymer chains. The augmented Gent model is widely accepted as one which qualitatively captures the behavior of dielectric elastomers (Li et al., 2013; Zhou et al., 2014; Wang et al., 2016).

We consider a matrix whose properties are

$$\rho^{(m)} = 1000\,\mathrm{kg/m^3}, \quad \mu^{(m)} = 200\mathrm{kPa}, \quad \epsilon_r^{(m)} = 3, \quad J_m^{(m)} = 10, \tag{49}$$

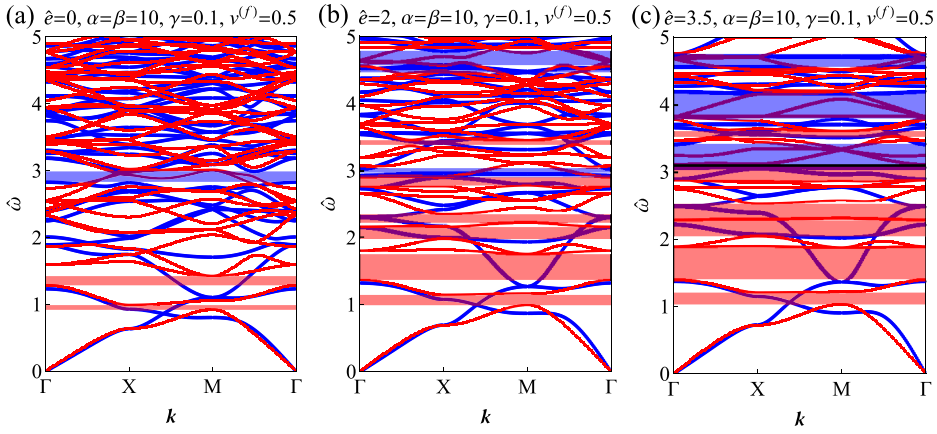

Fig. 2. Band diagrams of DG composite with circular fibers, subjected to the normalized electric bias fields (a) $\hat{e}=0$, (b) $\hat{e}=2$ and (c) $\hat{e}=3.5$. Normalized frequencies $\hat{\omega}$ are shown as functions of the reduced wave vector $\mathbf{k}$ along $\Gamma XM\Gamma$, where the blue and red curves correspond to in-plane and anti-plane normalized frequencies, respectively. Blue, red and black regions correspond to the in-plane, anti-plane and complete gaps, respectively. The composite properties are $\rho^{(m)}=\rho^{(f)}=1000\,\mathrm{kg/m^3}$, $\mu^{(m)}=200\,\mathrm{kPa}$, $\epsilon_r^{(m)}=3$, $J_m^{(m)}=10$, $\alpha=10$, $\beta=10$, $\gamma=0.1$ and $\nu^{(f)}=0.5$ (For interpretation of the references to colour in this figure legend, the reader is referred to the web version of this article.)

which are characteristic values for soft dielectrics (Kornbluh and Pelrine, 2008). Setting $J_m=10$ reflects a limiting uniaxial stretch of 3.5. We fix $\rho^{(f)}=\rho^{(m)}$, and examine different composites by varying the remaining fiber properties. This is carried out by changing the fiber volume fraction $\nu^{(f)}$, shear contrast parameter $\alpha=\mu^{(f)}/\mu^{(m)}$, permittivity contrast parameter $\beta=\epsilon^{(f)}/\epsilon^{(m)}$, and the locking contrast parameter $\gamma=J_m^{(f)}/J_m^{(m)}$. Note that when $\gamma<1$ the limiting strain of the fibers is smaller than the matrix, and hence they stiffen faster than the matrix; when $\gamma>1$, the limiting strain of the matrix is smaller than the fibers, and hence the matrix stiffens faster than the fibers.

We start with an exemplary composite characterized by $\alpha=10$, $\beta=10$, $\gamma=0.1$ and $\nu^{(f)}=0.5$. We plot its normalized eigenfrequencies $\hat{\omega}=\omega A/2\pi c$, where $c=\sqrt{\mu^{(m)}/\rho^{(m)}}$ is the shear wave velocity in the undeformed matrix, as functions of the reduced wave vector $\mathbf{k}$ along $\Gamma XM\Gamma$, at different electric fields. Specifically, Figs. 2a–c corresponds to $\hat{e}=0$, 2 and 3.5, respectively.

Herein and henceforth, blue, red and black regions denote gaps in the in-plane mode, anti-plane mode and their intersection, respectively. In other words, displacements perpendicular to the fibers (resp. along the fibers) at frequencies associated with the blue bands (resp. red bands) cannot propagate. Waves at frequencies pertaining to the black bands are annihilated, irrespective of the direction of the displacements and the direction of the wavefront. Thus, such frequencies constitute *complete* band gaps. The existence of complete gaps highly depends on the composition of the composite and the external load. Herein, a complete gap is achieved at $\hat{e}=3.5$, covering the normalized frequencies $3.08\lesssim\hat{\omega}\lesssim3.11$. A comparison of Figs. 2a–c reveals the effect of the bias electric field: as $\hat{e}$ is enhanced, the spectrum is shifted towards higher frequencies, while the number of gaps is increased and their width expands. Thus, the relative width of the gaps in the spectrum, which we refer to as the *gap density*, increases. Fig. 2 also shows that gaps associated with the in-plane mode open at higher frequencies than those associated with the anti-plane mode.

Fig. 3 shows the prohibited normalized frequencies as functions of the fiber volume fraction $\nu^{(f)}$ at $\alpha=10$, $\beta=10$, $\gamma=1$ and $\hat{e}=2$. The in-plane and anti-plane gaps open at $\nu^{(f)}=0.14$ and 0.35, respectively. The gaps close at $\nu^{(f)}=0.61$ and 0.76 for the in-plane and anti-plane modes, respectively. The second in-plane and anti-plane gaps are the widest, with a width $\Delta\hat{\omega}=0.19$, at $\nu^{(f)}=0.48$ and 0.58, respectively.

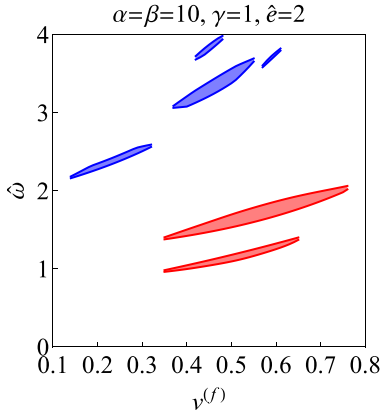

Fig. 3. Prohibited normalized frequencies as functions of the fiber volume fraction $\nu^{(f)}$. Blue and red regions correspond to in-plane, anti-plane and complete gaps, respectively. The composite properties are $\rho^{(m)}=\rho^{(f)}=1000\,\mathrm{kg/m^3}$, $\mu^{(m)}=200\mathrm{kPa}$, $\epsilon_r^{(m)}=3$ and $J_m^{(m)}=10$, $\alpha=10$, $\beta=10$ and $\gamma=1$. The normalized bias electric field is $\hat{e}=2$ (For interpretation of the references to colour in this figure legend, the reader is referred to the web version of this article.)

Fig. 4 shows prohibited normalized frequencies as functions of the shear contrast α. Specifically, Fig. 4a corresponds to $\beta=10$, $\gamma=1$, $\nu^{(f)}=0.5$ and $\hat{e}=2$; Fig. 4b corresponds $\beta=10$, $\gamma=0.1$, $\nu^{(f)}=0.5$ and $\hat{e}=2$, and Fig. 4c corresponds to $\beta=10$, $\gamma=0.1$, $\nu^{(f)}=0.5$ and $\hat{e}=3.5$. Fig. 4a demonstrates how the number and width of the anti-plane gaps increase monotonically with α. By contrast, the first in-plane gap widens up to a maximal value at $\alpha\simeq10$, and closes at $\alpha\simeq17$. In that interval, two additional in-plane gaps open. Nevertheless, in-plane gap density decreases beyond $\alpha\simeq15$. A further examination beyond the plotted range of α shows it increases again at $\alpha>25$. Contrarily, there is no decrease in the gap density when $\gamma=0.1$ (Fig. 4b). Fig. 4c shows that when $\gamma=0.1$ and $\hat{e}=3.5$, the dependency of the band diagram on α is very weak; we postpone an explanation for the variance in the dependency on α to the end of the section. Fig. 4a shows that when there is no contrast in the locking parameter, a minimal value of shear contrast is required for the opening of the gaps. By contrast, when $\gamma=0.1$ and $\hat{e}=2$ there are anti-plane gaps even when $\alpha=1$; when $\gamma=0.1$ and $\hat{e}=3.5$ there are also in-plane gaps when $\alpha=1$. A complete gap is observed in Fig. 4c, when $\beta=10$, $\gamma=0.1$, $\nu^{(f)}=0.5$ and $\hat{e}=3.5$. At $\alpha=1$, its width and middle frequency are $\Delta\hat{\omega}\simeq0.03$ and $\hat{\omega}\simeq3.11$, respectively.

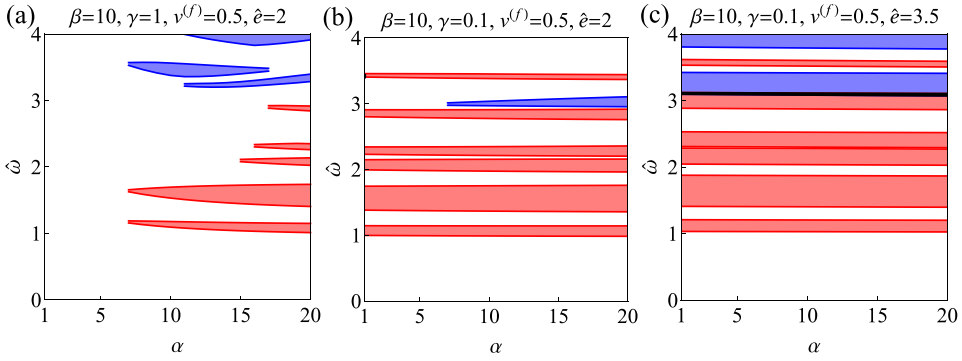

Fig. 4. Prohibited normalized frequencies as functions of the shear contrast α. Blue, red and black regions correspond to in-plane, anti-plane and complete gaps, respectively. The composite properties are $\rho^{(m)}=\rho^{(f)}=1000\,\mathrm{kg/m^3}$, $\mu^{(m)}=200\mathrm{kPa}$, $\epsilon_r^{(m)}=3$ and $J_m^{(m)}=10$, where (a) $\beta=10$, $\gamma=1$, $\nu^{(f)}=0.5$, $\hat{e}=2$, (b) $\beta=10$, $\gamma=0.1$, $\nu^{(f)}=0.5$, $\hat{e}=2$, and (c) $\beta=10$, $\gamma=0.1$, $\nu^{(f)}=0.5$, $\hat{e}=3.5$ (For interpretation of the references to colour in this figure legend, the reader is referred to the web version of this article.)

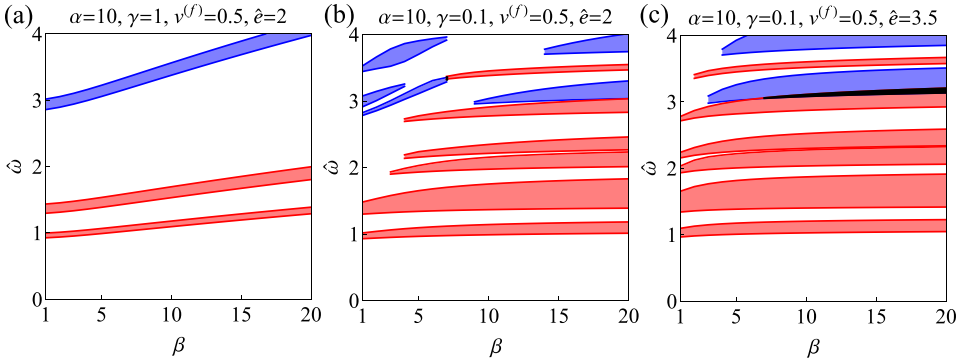

Fig. 5. Prohibited normalized frequencies as functions of the permittivity contrast β. Blue, red and black regions correspond to in-plane, anti-plane and complete gaps, respectively. The composite properties are $\rho^{(m)}=\rho^{(f)}=1000\,\mathrm{kg/m^3}$, $\mu^{(m)}=200\mathrm{kPa}$, $\epsilon_r^{(m)}=3$ and $J_m^{(m)}=10$, where (a) $\alpha=10$, $\gamma=1$, $\nu^{(f)}=0.5$, $\hat{e}=2$, (b) $\alpha=10$, $\gamma=0.1$, $\nu^{(f)}=0.5$, $\hat{e}=2$, and (c) $\alpha=10$, $\gamma=0.1$, $\nu^{(f)}=0.5$, $\hat{e}=3.5$ (For interpretation of the references to colour in this figure legend, the reader is referred to the web version of this article.)

While at $\alpha=20$ it widens by about 36%, the middle frequency of the gap is lower by about 10%.

Fig. 5 shows prohibited normalized frequencies as functions of the permittivity contrast β. Specifically, Figs. 5a–c, correspond to $\alpha=10$, $\gamma=1$, $\nu^{(f)}=0.5$ and $\hat{e}=2$, $\alpha=10$, $\gamma=0.1$, $\nu^{(f)}=0.5$ and $\hat{e}=2$, and $\alpha=10$, $\gamma=0.1$, $\nu^{(f)}=0.5$ and $\hat{e}=3.5$, respectively. At $\gamma=1$ (Fig. 5a), one in-plane gap and two anti-plane gaps appear; these become wider and move towards higher frequencies as β increases. Again, we postpone an explanation of this trend to the end of the section. Figs. 5b and c show that at $\gamma=0.1$, the anti-plane gap density increases as β increases, regardless of the value of $\hat{e}$. At $\hat{e}=3.5$, the in-plane gap density increases monotonically with β; when $\hat{e}=2$, it increases until $\beta\simeq 5$, then decreases until $\beta\simeq 8$, and increases again beyond that value. Similar to the dependency on shear contrast, the effect of β on the gap density is more pronounced at $\gamma=1$ and lower bias electric fields. Contrarily to the dependency on α, no minimal permittivity contrast is required for the opening of the gaps. Moreover, when $\gamma=0.1$, a complete gap opens at $\hat{\omega}\simeq 3.05$, when $\beta\simeq 7$, at which $\lambda\simeq 1.33$, and increases monotonically with β.

Fig. 6 illustrates prohibited normalized frequencies as functions of the locking contrast γ. The fiber properties are $\alpha=10$, $\beta=10$, $\nu^{(f)}=0.5$. The electric bias field in Figs. 6a and b is $\hat{e}=2$ and 3.5, respectively. We observe a monotonic decrease in the anti-plane gap density as a function of γ. The dependency of the in-plane gaps is more complicated; it decreases at low and high values of γ, and increases at the intervals $0.15\lesssim\gamma\lesssim 0.4$ and $0.5\lesssim\gamma\lesssim 0.75$, when $\hat{e}=2$ and 3.5, respectively. Two narrow complete gaps appear in Fig. 6a ($\hat{e}=2$), across $2.96\lesssim\hat{\omega}\lesssim 3$ and $3.40\lesssim\hat{\omega}\lesssim 3.44$. When $\hat{e}=3.5$ (Fig. 6b), there is a single complete gap, starting

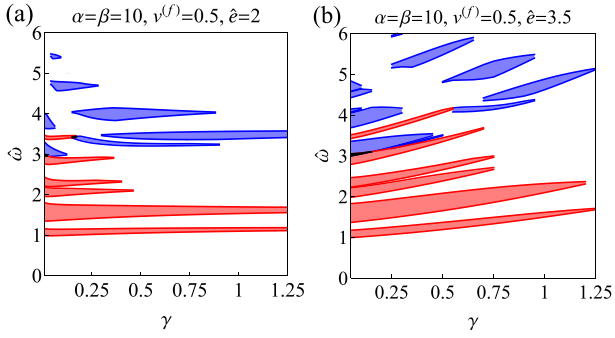

Fig. 6. Prohibited normalized frequencies as functions of the locking contrast γ. Blue, red and black regions correspond to in-plane, anti-plane and complete gaps, respectively. The composite properties are $\rho^{(m)}=\rho^{(f)}=1000\,\mathrm{kg/m^3}$, $\mu^{(m)}=200\mathrm{kPa}$, $\epsilon_r^{(m)}=3$ and $J_m^{(m)}=10$, where (a) $\alpha=10$, $\beta=10$, $\nu^{(f)}=0.5$ and $\hat{e}=2$, and (b) $\alpha=10$, $\beta=10$, $\nu^{(f)}=0.5$ and $\hat{e}=3.5$ (For interpretation of the references to colour in this figure legend, the reader is referred to the web version of this article.)

at $3.05\lesssim\hat{\omega}\lesssim 3.15$, which closes when $\gamma\simeq 0.18$. The central frequency of the first anti-plane gap is $\hat{\omega}\simeq 1.07$, and its width is $\Delta\hat{\omega}\simeq 0.17$. When $\hat{e}=2$, it vanishes beyond the plotted range, at $\gamma\simeq 4$ and $\hat{\omega}\simeq 1.17$; when $\hat{e}=3.5$, it vanishes at $\gamma\simeq 1.25$ and $\hat{\omega}\simeq 1.7$. There is no opening of new anti-plane gaps after the first gap closes.

From the tunability perspective, the most important dependency is on the electric field; all other parameters are fixed once a composite is manufactured, while the electric field is adjustable. This dependency is explored in Fig. 7, which shows prohibited

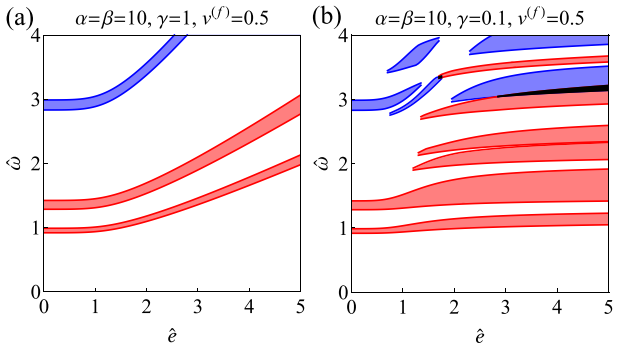

Fig. 7. Prohibited normalized frequencies as functions of the normalized electric bias field $\hat{e}$. Blue, red and black regions correspond to in-plane, anti-plane and complete gaps, respectively. The composite properties are $\rho^{(m)}=\rho^{(f)}=1000\,\mathrm{kg/m^3}$, $\mu^{(m)}=200\mathrm{kPa}$, $\epsilon_r^{(m)}=3$ and $J_m^{(m)}=10$, where (a) $\alpha=10$, $\beta=10$, $\gamma=1$, $\nu^{(f)}=0.5$, and (b) $\alpha=10$, $\beta=10$ $\gamma=0.1$, $\nu^{(f)}=0.5$. (For interpretation of the references to colour in this figure legend, the reader is referred to the web version of this article.)

normalized frequencies as functions of $\hat{e}$, at representative values $\alpha=10$, $\beta=10$ and $\nu^{(f)}=0.5$. Figs. 7a and b correspond to $\gamma=1$ and 0.1, respectively. When $\gamma=0.1$, a complete gap opens at $\hat{\omega}\simeq 3$ and $\hat{e}\simeq 2.85$, for which $\lambda\simeq 1.33$, and increases monotonically with $\hat{e}$. Contrarily, when $\gamma=1$ there are no complete gaps. As the electric field is enhanced, the gaps are shifted towards higher frequencies, while their total density is increased by opening of new gaps and enlargement of existing ones. At $\hat{e}=0$, regardless of the value of γ, the width of the first anti-plane gap is $\Delta\hat{\omega}\simeq 0.07$ and its middle frequency is $\hat{\omega}\simeq 0.95$; the width of the 1st in-plane gap is $\Delta\hat{\omega}\simeq 0.16$ and its middle frequency is $\hat{\omega}\simeq 2.91$. At $\gamma=1$ and $\hat{e}=5$, the width of the first anti-plane gap is $\Delta\hat{\omega}\simeq 0.15$ and its middle frequency is $\hat{\omega}\simeq 2.06$. The width of the first in-plane gap is $\Delta\hat{\omega}\simeq 0.34$ and its middle frequency is $\hat{\omega}\simeq 6.28$ (outside the plotted range). Thus, for both modes, the width increases by approximately 115%, and the middle frequency increases about the same value. At $\gamma=0.1$ and $\hat{e}=5$, the width of the first anti-plane gap is $\Delta\hat{\omega}\simeq 0.18$ and its middle frequency is $\hat{\omega}\simeq 1.14$. Thus, the width increases by approximately 155% and its middle frequency increases by about 20%. At $\gamma=0.1$, the first in-plane gap closes at $\hat{e}\simeq 1.35$ when $\hat{\omega}\simeq 3.4$, hence the middle frequency increases by about 10%. The width and central frequency of the lowest in-plane gap at $\hat{e}=5$ are $\Delta\hat{\omega}\simeq 0.38$ and $\hat{\omega}\simeq 3.33$, respectively. The width is approximately a third wider and 15% higher than the width at $\hat{e}=0$.

To explain the different dependencies on the composite parameters and electric load, we recall that the fundamental quantity that governs the gap density is the mismatch between the impedance of each phase. In the examples presented, the phases have the same mass density; this density does not vary with the deformation, on account of incompressibility. Therefore, the mismatch depends on the pertinent stiffness, *i.e.,* the quantities that multiply the spatial derivative of the displacement in the governing equations. Eq. (35) shows that $\hat{\mu}^{(p)}$ is that stiffness for the in-plane mode. The identification of the corresponding stiffness for the anti-plane mode is more complicated, as the displacement field is coupled with the electric field through Eqs. (34c) and (34d). This coupling manifests itself in the components of $\tilde{Q}$ in Eq. (47). Interestingly, we find that the contribution of $Q^{(1,2)}Q^{(2,2)^{-1}}Q^{(2,1)}$ cancels the part of $Q^{(1,1)}$ which explicitly depends on e_2^2. Moreover, we find that this result applies to any material which depends on I_1 and I_{5e} in a separable form, even when the dependency on I_1 and I_{5e} is via any nonlinear function. Details regarding this result are given in Appendix D. Accordingly, we arrive at the same stiffness for the anti-plane mode, namely, $\hat{\mu}^{(p)}$. We therefore define a measure of mismatch, η, as

$$\eta := \frac{1}{2}\left(\tilde{\alpha}+\tilde{\alpha}^{-1}\right), \tag{50}$$

where

$$\tilde{\alpha} := \frac{\hat{\mu}^{(f)}}{\hat{\mu}^{(m)}} = \alpha\frac{1-\left(2\lambda^2+\lambda^{-4}-3\right)/J_m^{(m)}}{1-\left(2\lambda^2+\lambda^{-4}-3\right)/\gamma J_m^{(m)}} \tag{51}$$

is referred to as the instantaneous shear contrast. The role of α, β, γ and $\hat{e}$ in the evolution of the gap density becomes clearer—a change in these quantities modifies the stretch ratio λ non-linearly via

$$\left(\frac{\alpha\nu^{(f)}}{1-\frac{2\lambda^2+\lambda^{-4}-3}{\gamma J_m^{(m)}}}+\frac{\nu^{(m)}}{1-\frac{2\lambda^2+\lambda^{-4}-3}{J_m^{(m)}}}\right)(\lambda^2-\lambda^{-4})=\frac{\nu^{(f)}\beta+\nu^{(m)}}{\epsilon^{(m)}}\hat{e}^2, \tag{52}$$

and, in turn, modifies η. This dependency is illustrated in Fig. 8. Specifically, Figs. 8a–d show the measure of mismatch η, as a function of α, β, γ and $\hat{e}$, respectively. The free parameters in each figure are $\alpha=10$, $\beta=10$, $\gamma=0.1$ and $\nu^{(f)}=0.5$, while the electric bias field is $\hat{e}=3.5$. The corresponding value of λ is showed on the upper axes.

We observe that η increases monotonically with α, β and $\hat{e}$, in agreement with the increase in the gap density observed in Figs. 4, 5 and 7. Fig. 8c shows that η decreases with γ, until $\eta=1$ at $\gamma\simeq 8.5$, beyond which η slightly increases. This decrease of η is in agreement with the closure of the gaps in Fig. 6b. We observe that the relative change in η correlates with the relative change in the gap density—when the increment in η is small with respect to its value, the change in the gap density is barely noticeable (Figs. 4c and 8a); when the increment in η is significant, a much greater change in the gap density is observed (Figs. 7b and 8d).

When the phases have the same locking parameter, *i.e.*, $\gamma=1$, the instantaneous shear contrast $\tilde{\alpha}$ is independent of the deformation and equals α. Accordingly, η and the gap density are independent of β, $\hat{e}$ and λ. However, the whole spectrum is stretched with the stiffening of the composite caused by the deformation. Accordingly, the gaps in Figs. 5a and 7a are wider at large values of β and $\hat{e}$, while their relative size in the frequency domain remains the same. We refer the reader to video 1a in the supplementary material online, illustrating the change of the corresponding spectrum as a function of $\hat{e}$, when $\gamma=1$. This observation is in agreement with the findings of Shmuel and Band (2016) for finitely deformed laminates. When $\gamma\neq 1$, the spectrum changes in an intricate manner with the electric field, such that the order of the eigenmodes is changed. For instance, the third mode at $\alpha=10$, $\beta=10$, $\gamma=0.1$, $\nu^{(f)}=0.5$ and $\hat{e}=0$ between Γ and X becomes the fourth mode when $\hat{e}\simeq 1.45$. This shuffle in the ordering of the eigenmodes is accompanied by the closure of certain gaps and the opening of others. We refer the reader again to video 1b, showing the evolution of the pertinent spectrum as function of the electric field when $\gamma=0.1$; therein, this transition is evident. Video 2 in the supplementary material online revisits the in-plane band diagram as a function of the electric field. Therein, the vertical axis is scaled as follows. The normalized frequencies are divided by the frequency of a chosen mode calculated at Γ for each applied electric field. Thus, videos 2a and 2b show the scaled frequencies at γ=1 and 0.1, respectively. Thereby, the stretching of the spectrum is factored out. Indeed, video 2a demonstrates that when η is fixed (γ=1), the relative size of the gaps is fixed too, and the widening of the gaps is only due to the stretching of the spectrum. By contrast, video 2a illustrates that when η changes non-monotonically (γ=0.1), the relative size of the gaps changes non-monotonically too. Moreover, we observe how the structure of the

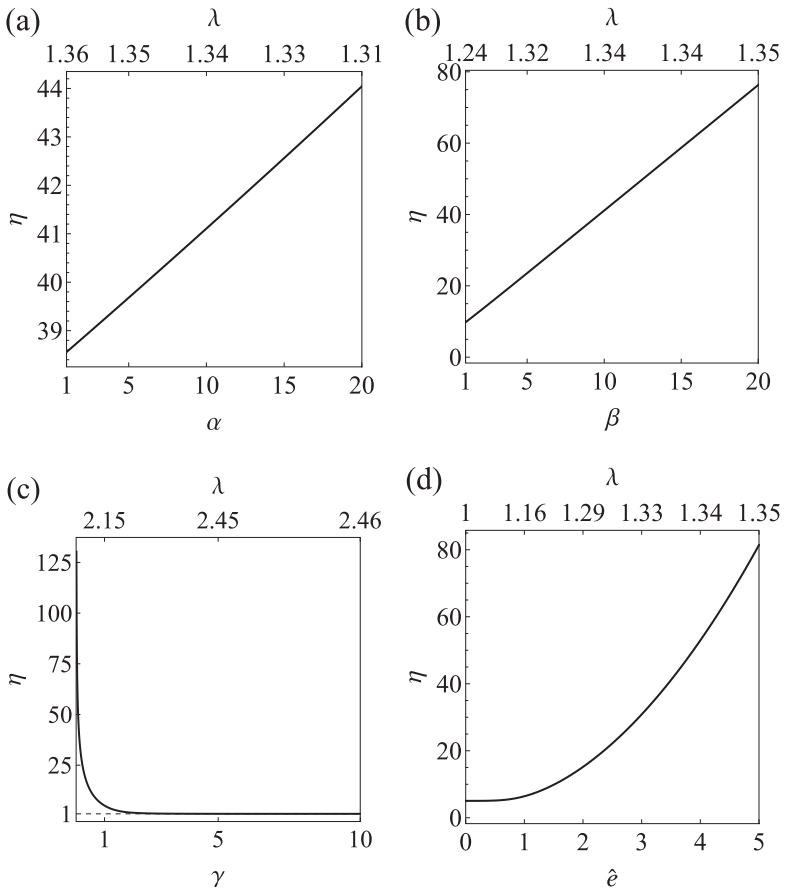

Fig. 8. The mismatch impedance η as a function of (a) the normalized electric bias field $\hat{e}$, (b) the permittivity contrast β, (c) the shear contrast α, and (d) the locking parameter contrast γ. The free parameters in each Fig. are $\alpha = 10$, $\beta = 10$, $\gamma = 0.1$, $\nu^{(f)} = 0.5$ and $\hat{e} = 3.5$. Corresponding in-plane stretch λ is shown on the top axes.

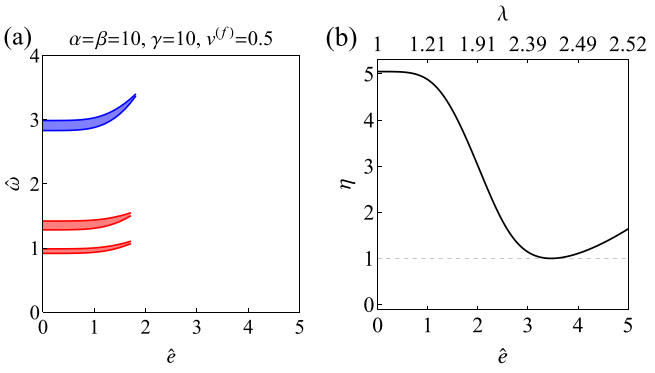

Fig. 9. (a) Prohibited normalized frequencies as functions of the electric bias field $\hat{e}$. Blue, red and black regions correspond to in-plane, anti-plane and complete gaps, respectively. (b) The mismatch impedance η as a function of the normalized electric bias field $\hat{e}$. The corresponding in-plane stretch is shown on the top axis. The composite properties are $\rho^{(m)} = \rho^{(f)} = 1000\,\mathrm{kg/m^3}$, $\mu^{(m)} = 200\mathrm{kPa}$, $\epsilon_r^{(m)} = 3$, $J_m^{(m)} = 10$, $\alpha = 10$, $\beta = 10$, $\gamma = 10$ and $\nu^{(f)} = 0.5$ (For interpretation of the references to colour in this figure legend, the reader is referred to the web version of this article.)

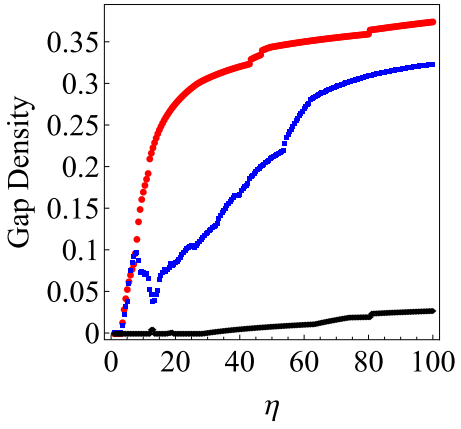

Fig. 10. Gap densities as functions of the impedance mismatch η. Blue, red and black curves correspond to the in-plane, anti-plane and complete gaps, respectively. The composite properties are $\rho^{(m)} = \rho^{(f)} = 1000\,\mathrm{kg/m^3}$, $\mu^{(m)} = 200\mathrm{kPa}$, $\epsilon_r^{(m)} = 3$ and $J_m^{(m)} = 10$. (For interpretation of the references to colour in this figure legend, the reader is referred to the web version of this article.)

diagram changes in an intricate manner, through the shuffling of the eigenmodes.

In view of the above observations, we choose to illustrate in Fig. 9 the correlation between η and the gap density, with the following example. We revisit the gap density as a function of $\hat{e}$ in Fig. 9a, this time with $\gamma = 10$, and display corresponding values of η and λ in Fig. 9b. The properties of the composite are $\alpha = 10$, $\beta = 10$, $\gamma = 10$ and $\nu^{(f)} = 0.5$. The gaps in Fig. 9a are narrowed with increasing values of $\hat{e}$, until they close at $\hat{e} \simeq 1.85$. This process is associated with the reduction of η when $\hat{e}$ increases, as depicted in Fig. 9b. The dependency of η on $\hat{e}$ is reversed beyond $\hat{e} \simeq 3.2$. This non-monotonicity results from a competition between the initial shear contrast and the stiffening of the matrix. In other words, $\tilde{\alpha} = \alpha > 1$ when no electric field is applied, for which the fibers are stiffer than the matrix; by application of electric load, the matrix stiffens faster than the fibers since $\gamma > 1$, and therefore the impedance mismatch reduces as $\tilde{\alpha} < \alpha$. At $\hat{e} \simeq 3.2$, we obtain $\hat{\mu}^{(f)} = \hat{\mu}^{(m)}$ and thus $\eta = 1$. Beyond $\hat{e} \simeq 3.2$, $\hat{\mu}^{(m)} > \hat{\mu}^{(f)}$

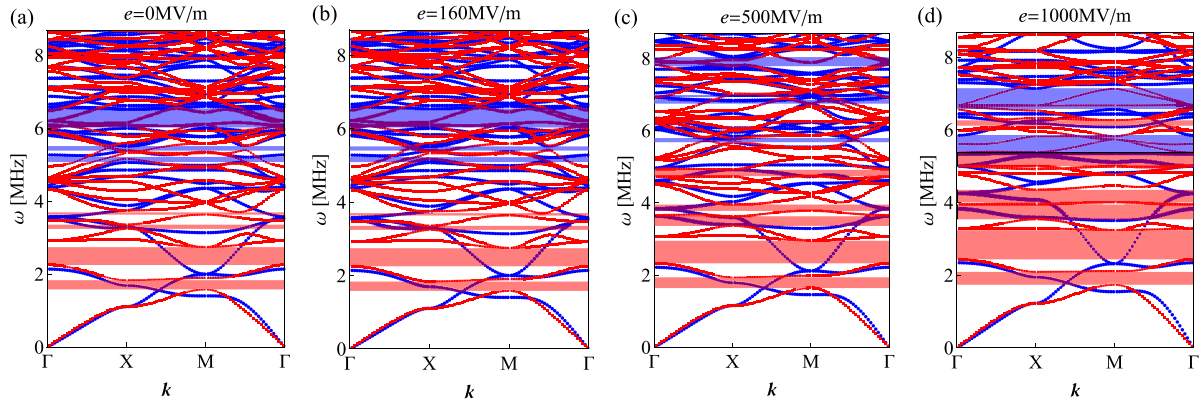

Fig. 11. Band diagrams of a composite made of Silicone CF19-2186 matrix and circular Polyurethane PT6100S fibers. The initial radius of the fibers is $R = 25\,\mu$m, and their volume fraction is $\nu^{(f)} = 0.5$. The composite is subjected to the electric bias fields (a) $e = 0$MV/m, (b) $e = 100$MV/m, (c) $e = 500$MV/m and (d) $e = 1000$MV/m. The in-plane (blue curves) and anti-plane (red curves) eigenfrequencies ω are shown as functions of the reduced wave vector $\mathbf{k}$ along $\Gamma X M \Gamma$. Blue, red and black regions correspond to in-plane, anti-plane and complete gaps, respectively (For interpretation of the references to colour in this figure legend, the reader is referred to the web version of this article.)

Table 1
Physical properties of Silicone CF19-2186 and polyurethane PT6100S.

Material	ρ (kg/m^3)	μ (kPa)	ϵ_r	J_m	Dielectric strength (MV/m)
Silicone CF19-2186	1100	333	2.8	46.3	235
Polyurethane PT6100S	1200	5667	7	6.67	160

and a mismatch in the impedance is created again. This mismatch, however, is not large enough to reopen gaps in that examined frequency range.

Fig. 10 displays the gap density as function of η, using its approximation over a truncated interval of frequencies. Specifically, we have calculated the relative size of the gaps in an interval that ends with the frequency of the highest eigenmode calculated at Γ. We observe that there exists a threshold value of $\eta \simeq 3$, below which there are no gaps. The curve describing the density of the anti-plane gaps is a monotonic function of η, with a decreasing slope. By contrast, the in-plane gap density increases until $\eta \lesssim 7.5$, then decreases until $\eta \lesssim 13$, and then increases again. We have no explanation for the intermediate decrease; we speculate it is a result of the truncation of the frequency interval. We note that the density of the complete gaps increases monotonically with η.

We conclude the numerical investigation with a dimensional example, modeling the constituents with the properties of two of the commercial products used in the seminal paper of Pelrine et al. (2000a). Specifically, we use silicone CF19-2186 by Nusil to model the matrix, and polyurethane PT6100S by Deerfield to model the fibers. The material properties are given in Table 1; therein, the shear modulus, dielectric constant and dielectric strength—the electric field at which the material begins to conduct charge—were taken from Pelrine et al. (2000a), the mass density is taken from the website of the manufacturers Dotmar[2] and Nusil,[3] and the locking parameter was calculated using the elongation at failure to estimate the limiting stretch. The fibers are taken with an initial radius of $R = 25\,\mu$m and a volume fraction of $\nu^{(f)} = 0.5$, for which the referential lattice parameter is $A \simeq 66.06\,\mu$m. Fig. 11 displays the dimensional eigenfrequencies ω as functions of the reduced wave vector $\mathbf{k}$ along $\Gamma X M \Gamma$, at different electric fields. Specifically, Figs. 11a–d correspond to $e = 0$MV/m, 160MV/m, 500MV/m and 1000MV/m, respectively. These electric fields induce the in-plane stretch ratios $\lambda = 1$, 1.067, 1.602 and 1.986, respectively. The existence of band-gaps without the application of electric load is observed in Fig. 11a. Therein, anti-plane gaps appear across the frequencies 1.58 MHz $\lesssim \omega \lesssim$ 1.83 MHz, 2.25 MHz $\lesssim \omega \lesssim$ 2.74 MHz, 3.24 MHz $\lesssim \omega \lesssim$ 3.36 MHz and 3.63 MHz $\lesssim \omega \lesssim$ 3.69 MHz; three in-plane gaps appear across the frequencies 5.07 MHz $\lesssim \omega \lesssim$ 5.21 MHz, 5.39 MHz $\lesssim \omega \lesssim$ 5.51 MHz and 6.02 MHz $\lesssim \omega \lesssim$ 6.54 MHz. The electric field considered in Fig. 11b, $e = 160$MV/m, corresponds to onset of the polyurethane electric breakdown observed in Pelrine et al. (2000a). Since the resultant stretch is relatively small, there is only a minor change in the band diagram.

Exploring electric loads beyond the dielectric strength reported by Pelrine et al. (2000a) purportedly seems superfluous. However, research conducted after the aforementioned early work shows that the dielectric strength can be increased in different ways, such as oil-encapsulation (Lau et al., 2015), modification of the elastomer synthesis at the molecular level (Madsen et al., 2014; 2015), and pre-stretching (Kofod, 2008; Huang et al., 2012; Gatti et al., 2014), which also improves actuation. Accordingly, we evaluate the band diagrams at greater electric fields and larger resultant stretches in Figs. 11c and 11 d. At $e = 500$MV/m and resultant stretch $\lambda = 1.602$ (Fig. 11c), the anti-plane gap-density increases, while the in-plane gap-density decreases. The first anti-plane gap covers now the frequencies 1.64 MHz $\lesssim \omega \lesssim$ 1.94 MHz, while the first in-plane gap is across the frequency range 5.68 MHz $\lesssim \omega \lesssim$ 5.80 MHz. Thus, the gaps are shifted towards higher frequencies, while the anti-plane gap widens, and the in-plane gap becomes more narrow. At $e = 1000$MV/m and the significant resultant stretch of $\lambda = 1.986$, the gap-density of both modes further increases. Moreover, a complete gap forms across the frequencies 5.36 MHz $\lesssim \omega \lesssim$ 5.37 MHz.

6. Concluding remarks

Motivated by industrial demand for active isolators and wave directors, we have explored the tunability of stopbands in electroactive fiber composites. Our investigation comprises the following steps and results. We have analytically determined the static response of soft incompressible dielectric fiber composites to an electric field along the fibers. Our solution holds for arbitrary fiber cross-sections, and any phases which are constitutively nonlinear in the manner described by Eq. (23). Thereby, we generalize the result of Shmuel (2013), by accounting for materials whose permittivity changes with deformations, and their dependency on I_1 is general. Subsequently, we have formulated the equations

[2] http://www.dotmar.com.au.
[3] http://nusil.com.

governing general linear motions propagating in the deformed composite, thus complementing the anti-plane analysis in Shmuel (2013). We have found that the anti-plane component of the displacement and the electric perturbation are coupled with each other, however decouple from the in-plane components of motion. Employing a plane wave expansion approach, we have derived a generalized eigenvalue system to determine the motion and the electric perturbation. We have explored numerical solutions of this system, to study how the band structure depends on the constituent properties and on the electrostatic field. To account for the finite extensibility of the polymer chains, we have used the augmented Gent energy when modeling the phases. The augmented Gent model uses three parameters: shear modulus, permittivity constant, and locking parameter; our results show that the band structure changes with the contrast between the shear modulus and permittivity constants of the phases, and correlates with η—an instantaneous measure of impedance mismatch. The bias electric field modifies η; accordingly, the bias field renders the band gaps tunable, by shifting them towards higher frequencies, and widening or narrowing the width, depending on the contrast between the locking parameter of each phase. Thus, when the limiting strain of the matrix is smaller than the limiting strain of the fibers, the band diagram evolves in a complicated manner with the applied electric field, due to a competition between the initial shear contrast and the rapid stiffening of the matrix. Our main finding is the existence of *complete* gaps, independent of the direction and plane of motion, at certain compositions and electric loadings. Together with previous works (*e.g.,* Shmuel and deBotton, 2013; Shmuel, 2015), the results above suggest the use of soft dielectrics as tunable waveguides and filters.

Acknowledgments

The authors acknowledge BSF (Grant No. 2014358) support. G.S. and R.G. also acknowledge ISF (Grant No. 1912/15) support.

Appendix A

The components of the constitutive tensors $\mathscr{A}$, $\mathscr{B}$ and $\mathscr{C}$ corresponding to the constitutive law (23) are (see, *e.g.*, Gei et al., 2014)

$$\mathscr{A}_{ij}^{(p)} = \frac{1}{\epsilon^{(p)}(\mathbf{x})}\varepsilon_{ij}^{-1} \tag{A.1}$$

$$\begin{aligned}\mathscr{B}_{ijk}^{(p)} &= \gamma_1(\delta_{jk}\varepsilon_{in}e_n + \varepsilon_{jn}e_n\delta_{ik}) \\ &\quad + \gamma_2(\delta_{ik}b_{jm}\varepsilon_{mn}e_n + b_{jk}\varepsilon_{in}e_n + b_{ik}\varepsilon_{jn}e_n + \delta_{jk}b_{im}\varepsilon_{mn}e_n),\end{aligned} \tag{A.2}$$

$$\begin{aligned}\mathscr{C}_{ijkl}^{(p)} &= \check{\zeta}^{(p)}(\mathbf{x})b_{ij}b_{kl} + \check{\mu}^{(p)}(\mathbf{x})\delta_{ik}b_{jl} + \gamma_1\epsilon^{(p)}(\mathbf{x})\delta_{ik}\varepsilon_{jn}e_n\varepsilon_{ls}e_s \\ &\quad + \gamma_2\epsilon^{(p)}(\mathbf{x})\delta_{ik}(\varepsilon_{ln}e_nb_{jm} + \varepsilon_{jn}e_nb_{lm})\varepsilon_{ms}e_s \\ &\quad + \gamma_2\epsilon^{(p)}(\mathbf{x})(b_{jl}\varepsilon_{kn}e_n + b_{jk}\varepsilon_{ln}e_n)\varepsilon_{is}e_s \\ &\quad + \gamma_2\epsilon^{(p)}(\mathbf{x})(b_{il}\varepsilon_{kn}e_n + b_{ik}\varepsilon_{ln}e_n)\varepsilon_{js}e_s,\end{aligned} \tag{A.3}$$

where $\check{\zeta}^{(p)}(\mathbf{x}) = 4\frac{\partial^2 W^{(p)}(\mathbf{x})}{\partial I_1^2}$ and $\check{\mu}^{(p)}(\mathbf{x}) = 2\frac{\partial W^{(p)}(\mathbf{x})}{\partial I_1}$.

Appendix B

The quantities $\hat{\mu}^{(p)}(\mathbf{x})$, $\tilde{\mu}^{(p)}(\mathbf{x})$, $\tilde{d}_2^{\,(p)}(\mathbf{x})$ and $\tilde{\epsilon}^{(p)}(\mathbf{x})$ abbreviate the following expressions

$$\hat{\mu}^{(p)}(\mathbf{x}) = \check{\mu}^{(p)}(\mathbf{x})\lambda^2, \tag{B.1}$$

$$\begin{aligned}\tilde{\mu}^{(p)}(\mathbf{x}) &= \hat{\mu}^{(p)}(\mathbf{x}) \\ &\quad + \left(\frac{\lambda^{10}\gamma_2^{(p)}}{(\hat{\gamma}^{(p)})^2} - \frac{\lambda^2(\gamma_2^{(p)}(1+\lambda^6) + \gamma_1^{(p)}\lambda^4)^2}{(\hat{\gamma}^{(p)})^2(\gamma_2^{(p)}\lambda^4 + \gamma_1^{(p)}\lambda^2 + \gamma_0^{(p)})}\right) \\ &\quad \times \epsilon^{(p)}(\mathbf{x})e_2^2,\end{aligned} \tag{B.2}$$

$$\tilde{d}_2^{\,(p)}(\mathbf{x}) = \left(\frac{\left(\gamma_2^{(p)}\left(\lambda^6+1\right) + \gamma_1^{(p)}\lambda^4\right)}{\lambda^2\left(\gamma_2^{(p)}\lambda^4 + \gamma_1^{(p)}\lambda^2 + \gamma_0^{(p)}\right)}\right)\epsilon^{(p)}(\mathbf{x})e_2, \tag{B.3}$$

$$\tilde{\epsilon}^{(p)}(\mathbf{x}) = \frac{\lambda^2}{\left(\gamma_0^{(p)} + \lambda^2\gamma_1^{(p)} + \lambda^4\gamma_2^{(p)}\right)}\epsilon^{(p)}(\mathbf{x}), \tag{B.4}$$

where $\hat{\gamma}^{(p)} = \lambda^8\gamma_0^{(p)} + \lambda^4\gamma_1^{(p)} + \gamma_2^{(p)}$. When specialized to the DG model, we have

$$\hat{\mu}^{(p)}(\mathbf{x}) = \frac{\lambda^2\mu^{(p)}(\mathbf{x})}{1 - \frac{2\lambda^2+\lambda^{-4}-3}{J_m^{(p)}(\mathbf{x})}}, \tag{B.5}$$

$$\tilde{\mu}^{(p)}(\mathbf{x}) = \hat{\mu}^{(p)}(\mathbf{x}) - \epsilon^{(p)}(\mathbf{x})e_2^2, \tag{B.6}$$

$$\tilde{d}_2^{\,(p)}(\mathbf{x}) = \epsilon^{(p)}(\mathbf{x})e_2 = d_2^{(p)}(\mathbf{x}), \tag{B.7}$$

$$\tilde{\epsilon}^{(p)}(\mathbf{x}) = \epsilon^{(p)}(\mathbf{x}). \tag{B.8}$$

Appendix C

The components $Q_{\mathbf{G},\mathbf{G}'}$, $R_{\mathbf{G},\mathbf{G}'}$, $Q_{\mathbf{G},\mathbf{G}'}^{(1,1)}$, $Q_{\mathbf{G},\mathbf{G}'}^{(1,2)}$, $Q_{\mathbf{G},\mathbf{G}'}^{(2,1)}$, $Q_{\mathbf{G},\mathbf{G}'}^{(2,2)}$, $R_{\mathbf{G},\mathbf{G}'}^{(1,1)}$ are

$$\begin{aligned}Q_{\mathbf{G},\mathbf{G}'} &= 4\hat{\mu}(\mathbf{G}-\mathbf{G}')(\mathbf{G}'+\mathbf{k})_1(\mathbf{G}'+\mathbf{k})_3(\mathbf{G}+\mathbf{k})_1(\mathbf{G}+\mathbf{k})_3 \\ &\quad + 4\hat{\mu}(\mathbf{G}-\mathbf{G}')\left[(\mathbf{G}'+\mathbf{k})_1^2 - (\mathbf{G}'+\mathbf{k})_3^2\right] \\ &\quad \times \left[(\mathbf{G}+\mathbf{k})_1^2 - (\mathbf{G}+\mathbf{k})_3^2\right],\end{aligned} \tag{C.1}$$

$$R_{\mathbf{G},\mathbf{G}'} = \rho(\mathbf{G}-\mathbf{G}')(\mathbf{G}'+\mathbf{k})\cdot(\mathbf{G}+\mathbf{k}), \tag{C.2}$$

$$Q_{\mathbf{G},\mathbf{G}'}^{(1,1)} = \tilde{\mu}(\mathbf{G}-\mathbf{G}')(\mathbf{G}'+\mathbf{k})\cdot(\mathbf{G}+\mathbf{k}), \tag{C.3}$$

$$Q_{\mathbf{G},\mathbf{G}'}^{(1,2)} = -\tilde{d}_2(\mathbf{G}-\mathbf{G}')(\mathbf{G}'+\mathbf{k})\cdot(\mathbf{G}+\mathbf{k}), \tag{C.4}$$

$$Q_{\mathbf{G},\mathbf{G}'}^{(2,1)} = Q_{\mathbf{G},\mathbf{G}'}^{(1,2)}, \tag{C.5}$$

$$Q_{\mathbf{G},\mathbf{G}'}^{(2,2)} = -\tilde{\epsilon}(\mathbf{G}-\mathbf{G}')(\mathbf{G}'+\mathbf{k})\cdot(\mathbf{G}+\mathbf{k}), \tag{C.6}$$

$$R_{\mathbf{G},\mathbf{G}'}^{(1,1)} = \rho(\mathbf{G}-\mathbf{G}'). \tag{C.7}$$

Appendix D

Consider an augmented energy of the form

$$\Psi = W_1(I_1) + W_5(I_{5e}), \tag{D.1}$$

such that $W_1(I_1)$ and $W_5(I_{5e})$ are nonlinear functions of I_1 and I_{5e}, respectively. Application of Eqs. (6), (10), and (11) provides

$$\mathbf{E} = \frac{\partial\Psi}{\partial\mathbf{D}} = \check{\epsilon}^{-1}\mathbf{C}\mathbf{D}, \tag{D.2}$$

$$\mathbf{P} = \frac{\partial\Psi}{\partial\mathbf{F}} = \check{\mu}\mathbf{F} + \check{\epsilon}^{-1}\mathbf{F}\mathbf{D}\otimes\mathbf{D} - p_0\mathbf{F}^{-\mathrm{T}}, \tag{D.3}$$

$$\mathbf{e} = \check{\epsilon}^{-1}\mathbf{d}, \tag{D.4}$$

$$\boldsymbol{\sigma} = \check{\mu}\mathbf{b} + \check{\epsilon}\mathbf{e}\otimes\mathbf{e} - p_0\mathbf{I}, \tag{D.5}$$

where $\check{\epsilon}^{-1} = 2\frac{\partial W_5}{\partial I_{5e}}$. Application of Eqs. (12) and (18) provides

$$\mathscr{A}_{ij} = \Lambda\check{\epsilon}^2 e_i e_j + \frac{1}{\check{\epsilon}}\delta_{ij}, \tag{D.6}$$

$$\mathscr{B}_{ijk} = \Lambda\check{\epsilon}^3 e_i e_j e_k + (e_i\delta_{jk} + e_j\delta_{ik}), \tag{D.7}$$

$$\mathscr{C}_{ijkl} = \varsigma b_{ij} b_{kl} + \check{\mu}\delta_{ik} b_{jl} + \Lambda\check{\epsilon}^4 e_i e_j e_k e_l + \check{\epsilon} e_j e_l \delta_{ik}, \tag{D.8}$$

where $\Lambda = 4\frac{\partial^2 W_5}{\partial I_{5e}^2}$ and $\varsigma = 4\frac{\partial^2 W_1}{\partial I_1^2}$.

By deriving the solution obtained in Section 3 with phases whose behavior is given by Eq. (D.1), the relation between the electric field and the stretch becomes

$$\overline{\check{\mu}^{(p)}}(\lambda^2 - \lambda^{-4}) = \overline{\check{\epsilon}^{(p)}} e_2^2, \tag{D.9}$$

where we recall that $\overline{(\bullet)} = v^{(f)}(\bullet)^{(f)} + v^{(m)}(\bullet)^{(m)}$. The quantities $\hat{\mu}^{(p)}(\mathbf{x})$, $\tilde{\mu}^{(p)}(\mathbf{x})$, $\tilde{d_2}^{(p)}(\mathbf{x})$ and $\tilde{\epsilon}^{(p)}(\mathbf{x})$ in the incremental governing equations accordingly read

$$\hat{\mu}^{(p)}(\mathbf{x}) = \lambda^2\check{\mu}^{(p)}(x_1, x_3), \tag{D.10}$$

$$\tilde{\mu}^{(p)}(\mathbf{x}) = \hat{\mu}^{(p)}(x_1 x_3) + \epsilon^{(p)}(x_1, x_3) e_2^2, \tag{D.11}$$

$$\tilde{d_2}^{(p)}(\mathbf{x}) = \check{\epsilon}^{(p)}(x_1, x_3) e_2, \tag{D.12}$$

$$\tilde{\epsilon}^{(p)}(\mathbf{x}) = \check{\epsilon}^{(p)}(x_1, x_3). \tag{D.13}$$

We observe that in a truncated plane wave expansion of equations based on such quantities, the corresponding matrix product $Q^{(1,2)}Q^{(2,2)^{-1}}Q^{(2,1)}$ counters the part in $Q^{(1,1)}$ that explicitly depends on e_2^2. We can show this analytically for finite numbers of plane waves, using a symbolic computation in Wolfram Mathematica 10. We were not able to prove it analytically for arbitrary numbers of plane waves; numerical investigation, however, supports the conjecture that this cancelation holds for arbitrary numbers of waves, and, in particular, the number of waves we used in Section 5, namely, 441.

Supplementary material

Supplementary material associated with this article can be found, in the online version, at 10.1016/j.ijsolstr.2016.10.002.

References

Arruda, E.M., Boyce, M.C., 1993. A three-dimensional constitutive model for the large stretch behavior of rubber elastic materials. J. Mech. Phys. Solids 41, 389–412.

Barnwell, E.G., Parnell, W.J., Abrahams, I.D., 2016. Antiplane elastic wave propagation in pre-stressed periodic structures; tuning, band gap switching and invariance. Wave Motion 63, 98–110. ISSN 0165–2125. http://dx.doi.org/10.1016/j.wavemoti.2016.02.001. URL http://www.sciencedirect.com/science/article/pii/S0165212516000111.

Bayat, A., Gordaninejad, F., 2015. Dynamic response of a tunable phononic crystal under applied mechanical and magnetic loadings. Smart Mater. Struct. 24 (6), 065027. URL http://stacks.iop.org/0964-1726/24/i=6/a=065027.

Benveniste, Y., Dvorak, G.J., 1992. Uniform fields and universal relations in piezoelectric composites. J. Mech. Phys. Solids 40 (6), 1295–1312. ISSN 0022–5096. http://dx.doi.org/10.1016/0022-5096(92)90016-U. URL http://www.sciencedirect.com/science/article/pii/002250969290016U.

Bertoldi, K., Boyce, M.C., 2008. Wave propagation and instabilities in monolithic and periodically structured elastomeric materials undergoing large deformations. Phys. Rev. B 78, 184107.

Bustamante, R., Ogden, R.W., 2006. Universal relations for nonlinear electroelastic solids. Acta Mech 182 (1), 125–140. ISSN 1619–6937. URL http://dx.doi.org/10.1007/s00707-005-0290-7.

Bustamante, R., Shariff, M.H.B.M., 2016. New sets of spectral invariants for electroelastic bodies with one and two families of fibres. Eur. J. Mech. A. Solids 58, 42–53. ISSN 0997–7538. http://dx.doi.org/10.1016/j.euromechsol.2016.01.006. URL http://www.sciencedirect.com/science/article/pii/S0997753816000073.

Castañeda, P.P., Siboni, M.H., 2012. A finite-strain constitutive theory for electro-active polymer composites via homogenization. Int. J. Non-Linear. Mech. 47 (2), 293–306.

Celli, P., Gonella, S., 2015. Manipulating waves with lego® bricks: a versatile experimental platform for metamaterial architectures. Appl. Phys. Lett. 107 (8), 081901. http://dx.doi.org/10.1063/1.4929566. URL http://scitation.aip.org/content/aip/journal/apl/107/8/10.1063/1.4929566.

Cohen, N., Dayal, K., deBotton, G., 2016. Electroelasticity of polymer networks. J. Mech. Phys. Solids. ISSN 0022–5096. http://dx.doi.org/10.1016/j.jmps.2016.03.022. URL http://www.sciencedirect.com/science/article/pii/S0022509615303525.

Cohen, N., deBotton, G., May 2016. Electromechanical interplay in deformable dielectric elastomer networks. Phys. Rev. Lett. 116, 208303. doi:10.1103/PhysRevLett.116.208303. URL http://link.aps.org/doi/10.1103/PhysRevLett.116.208303.

Craster, R.V., Antonakakis, T., Makwana, M., Guenneau, S., Sep. 2012. Dangers of using the edges of the Brillouin zone. Phys. Rev. B 86, 115130. doi:10.1103/PhysRevB.86.115130. URL http://link.aps.org/doi/10.1103/PhysRevB.86.115130.

Creegan, A., Anderson, I., 2014. 3D printing for dielectric elastomers. Proc. SPIE 9056. 905629–905629.

deBotton, G., Tevet-Deree, L., Socolsky, E.A., 2007. Electroactive heterogeneous polymers: analysis and applications to laminated composites. Mech. Adv. Mater. Struct. 14, 13–22.

Degraeve, S., Granger, C., Dubus, B., Vasseur, J.O., Thi, M.P., Hladky, A.-C., 2015. Tunability of bragg band gaps in one-dimensional piezoelectric phononic crystals using external capacitances. Smart Mater. Struct. 24 (8), 085013. URL http://stacks.iop.org/0964-1726/24/i=8/a=085013..

Dorfmann, A., Ogden, R.W., 2005. Nonlinear electroelasticity. Acta. Mech. 174, 167–183.

Dorfmann, A., Ogden, R.W., 2010. Electroelastic waves in a finitely deformed electroactive material. IM A. J. Appl. Math. 75, 603–636.

Feng, R., Liu, K., 2012. Tuning the band-gap of phononic crystals with an initial stress. Physica B 407 (12), 2032–2036. ISSN 0921–4526. http://dx.doi.org/10.1016/j.physb.2012.01.135. URL http://www.sciencedirect.com/science/article/pii/S0921452612001603..

Garcia-Pablos, D., Sigalas, M., de Espinosa, F.R.M., Torres, M., Kafesaki, M., Garcia, N., May 2000. Theory and experiments on elastic band gaps. Phys. Rev. Lett. 84, 4349–4352. URL http://link.aps.org/doi/10.1103/PhysRevLett.84.4349.

Gatti, D., Haus, H., Matysek, M., Frohnapfel, B., Tropea, C., Schlaak, H.F., 2014. The dielectric breakdown limit of silicone dielectric elastomer actuators. Appl. Phys. Lett. 104 (5), 052905. http://dx.doi.org/10.1063/1.4863816. URL http://scitation.aip.org/content/aip/journal/apl/104/5/10.1063/1.4863816.

Gei, M., Colonnelli, S., Springhetti, R., 2014. The role of electrostriction on the stability of dielectric elastomer actuators. Int. J. Solids Struct. 51 (3–4), 848–860. ISSN 0020–7683. http://dx.doi.org/10.1016/j.ijsolstr.2013.11.011. URL http://www.sciencedirect.com/science/article/pii/S0020768313004460.

Gei, M., Roccabianca, S., Bacca, M., 2011. Controlling bandgap in electroactive polymer-based structures. IEEE-ASME Trans. Mechatronics 16, 102–107.

Gent, A.N., 1996. A new constitutive relation for rubber. Rubber Chem. Technol. 69, 59–61.

Harrison, J.M., Kuchment, P., Sobolev, A., Winn, B., 2007. On occurrence of spectral edges for periodic operators inside the Brillouin zone. J. Phys. A 40 (27), 7597. URL http://stacks.iop.org/1751-8121/40/i=27/a=011.

Huang, J., Shian, S., Diebold, R.M., Suo, Z., Clarke, D.R., 2012. The thickness and stretch dependence of the electrical breakdown strength of an acrylic dielectric elastomer. Appl. Phys. Lett. 101 (12), 122905. http://dx.doi.org/10.1063/1.4754549. URL http://scitation.aip.org/content/aip/journal/apl/101/12/10.1063/1.4754549.

Huang, Y., Chen, W.Q., Wang, Y.S., Yang, W., 2015. Multiple refraction switches realized by stretching elastomeric scatterers in sonic crystals. AIP Adv. 5 (2), 027138. http://dx.doi.org/10.1063/1.4914018. URL http://scitation.aip.org/content/aip/journal/adva/5/2/10.1063/1.4914018.

Huang, Y., Zhang, C.L., Chen, W.Q., 2014. Tuning band structures of two-dimensional phononic crystals with biasing fields. J. Appl. Mech. 81 (9). 091008–091008. URL http://dx.doi.org/10.1115/1.4027915.

Kittel, C., 2005. Introduction to Solid State Physics. John Wiley & Sons, Inc., Hoboken, NJ.

Kofod, G., 2008. The static actuation of dielectric elastomer actuators: how does pre-stretch improve actuation? J. Phys. D 41 (21), 215–405.

Kornbluh, R., Pelrine, R., 2008. Dielectric elastomers as electromechanical transducers. In: chapter High-Performance Acrylic and Silicone Elastomers (Chapter 4). Elsevier, Oxford, UK, pp. 33–42.

Kushwaha, M.S., Halevi, P., Dobrzynski, L., Djafari-Rouhani, B., 1993. Acoustic band structure of periodic elastic composites. Phys. Rev. Lett. 71 (13), 2022–2025.

Kushwaha, M.S., Halevi, P., Martínez, G., Dobrzynski, L., Djafari-Rouhani, B., 1994. Theory of acoustic band structure of periodic elastic composites. Phys. Rev. B 49 (4), 2313–2322.

Lau, G.-K., Tan, D. D., La, T.-G., 2015. Large-strain, high-stress tubular dielectric elastomer actuator with high pre-stretch and oil encapsulation. URL http://dx.doi.org/10.1117/12.2084531.

Laude, V., Khelif, A., Benchabane, S., Wilm, M., Sylvestre, T., Kibler, B., Mussot, A., Dudley, J.M., Maillotte, H., Jan. 2005. Phononic band-gap guidance of acoustic modes in photonic crystal fibers. Phys. Rev. B 71, 045107. doi:10.1103/PhysRevB.71.045107. URL http://link.aps.org/doi/10.1103/PhysRevB.71.045107.

Lefèvre, V., Lopez-Pamies, O., 2015. The overall elastic dielectric properties of fiber-strengthened/weakened elastomers. J. Appl. Mech. 82 (11). 111009–111009. URL http://dx.doi.org/10.1115/1.4031187.

Li, T., Keplinger, C., Baumgartner, R., Bauer, S., Yang, W., Suo, Z., 2013. Giant voltage-induced deformation in dielectric elastomers near the verge of snap-through instability. J. Mech. Phys. Solids 61 (2), 611–628.

Liu, L., 2013. On energy formulations of electrostatics for continuum media. J. Mech. Phys. Solids 61 (4), 968–990. ISSN 0022–5096. http://dx.doi.org/10.1016/j.jmps.2012.12.007. URL http://www.sciencedirect.com/science/article/pii/S0022509613000033.

Lopez-Pamies, O., 2014. Elastic dielectric composites: theory and application to particle-filled ideal dielectrics. J. Mech. Phys. Solids 64, 61–82. ISSN 0022–5096. http://dx.doi.org/10.1016/j.jmps.2013.10.016. URL http://www.sciencedirect.com/science/article/pii/S0022509613002251.

Lu, T., Huang, J., Jordi, C., Kovacs, G., Huang, R., Clarke, D.R., Suo, Z., 2012. Dielectric elastomer actuators under equal-biaxial forces, uniaxial forces, and uniaxial constraint of stiff fibers. Soft Matter 8, 6167–6173. URL http://dx.doi.org/10.1039/C2SM25692D.

Madsen, F.B., Yu, L., Daugaard, A.E., Hvilsted, S., Skov, A.L., 2014. Silicone elastomers with high dielectric permittivity and high dielectric breakdown strength based on dipolar copolymers. Polymer (Guildf) 55 (24), 6212–6219. ISSN 0032–3861. http://dx.doi.org/10.1016/j.polymer.2014.09.056. URL http://www.sciencedirect.com/science/article/pii/S0032386114008623.

Madsen, F.B., Yu, L., Daugaard, A.E., Hvilsted, S., Skov, A.L., 2015. A new soft dielectric silicone elastomer matrix with high mechanical integrity and low losses. RSC Adv. 5, 10254–10259. doi:10.1039/C4RA13511C. URL http://dx.doi.org/10.1039/C4RA13511C.

Olhoff, N., Niu, B., Cheng, G., 2012. Optimum design of band-gap beam structures. Int J Solids Struct 49 (22), 3158–3169. ISSN 0020–7683. http://dx.doi.org/10.1016/j.ijsolstr.2012.06.014. URL http://www.sciencedirect.com/science/article/pii/S0020768312002715.

Pelrine, R., Kornbluh, R., Joseph, J., Heydt, R., Pei, Q.-B., Chiba, A., 2000. High-field deformation of elastomeric dielectrics for actuators. Mater. Sci. Eng. 11, 89–100.

Pelrine, R., Kornbluh, R., Pei, Q.-B., Joseph, J., 2000. High-speed electrically actuated elastomers with strain greater than 100%. Science 287, 836–839.

Qian, Z., Jin, F., Li, F., Kishimoto, K., 2008. Complete band gaps in two-dimensional piezoelectric phononic crystals with 1–3 connectivity family. Int. J. Solids Struct. 45 (17), 4748–4755.

Raney, J.R., Lewis, J.A., 2015. Printing mesoscale architectures. MRS Bull. 40, 943–950.

Ruzzene, M., Baz, A., 1999. Control of wave propagation in periodic composite rods using shape memory inserts. J. Vib. Acoust. 122 (2), 151–159. URL http://dx.doi.org/10.1115/1.568452.

Schneider, D., Liaqat, F., Boudouti, E.H.E., Hassouani, Y.E., Djafari-Rouhani, B., Tremel, W., Butt, H.-J., Fytas, G., 2012. Engineering the hypersonic phononic band gap of hybrid bragg stacks. Nano Lett. 12 (6), 3101–3108. PMID: 22506610. doi: http://dx.doi.org/10.1021/nl300982d. URL http://dx.doi.org/10.1021/nl300982d.

Shariff, M.H.B.M., 2011. Physical invariants for nonlinear orthotropic solids. Int. J. Solids Struct. 48 (13), 1906–1914. ISSN 0020–7683. http://dx.doi.org/10.1016/j.ijsolstr.2011.03.002. URL http://www.sciencedirect.com/science/article/pii/S0020768311000989.

Shen, L., Wu, J.H., Liu, Z., Fu, G., 2015. Extremely low-frequency lamb wave band gaps in a sandwich phononic crystal thin plate. Int. J. Mod. Phys. B 29 (05), 1550027. doi:10.1142/S0217979215500277. URL http://www.worldscientific.com/doi/abs/10.1142/S0217979215500277.

Shmuel, G., 2013. Electrostatically tunable band gaps in finitely extensible dielectric elastomer fiber composites. Int. J. Solids Struct. 50 (5), 680–686.

Shmuel, G., 2015. Manipulating torsional motions of soft dielectric tubes. J. Appl. Phys. 117 (17), 174902. http://dx.doi.org/10.1063/1.4919668. URL http://scitation.aip.org/content/aip/journal/jap/117/17/10.1063/1.4919668.

Shmuel, G., Band, R., 2016. Universality of the frequency spectrum of laminates. J. Mech. Phys. Solids 92, 127–136. ISSN 0022–5096. http://dx.doi.org/10.1016/j.jmps.2016.04.001. URL http://www.sciencedirect.com/science/article/pii/S002250961630134X.

Shmuel, G., deBotton, G., 2012. Band-gaps in electrostatically controlled dielectric laminates subjected to incremental shear motions. J. Mech. Phys. Solids 60, 1970–1981.

Shmuel, G., deBotton, G., 2013. Axisymmetric wave propagation in finitely deformed dielectric elastomer tubes. Proc. R. Soc. A 469 (2155).

Siboni, M.H., Avazmohammadi, R., Castañeda, P.P., 2014. Electromechanical instabilities in fiber-constrained, dielectric-elastomer composites subjected to all-around dead-loading. Math. Mech. Solids doi:10.1177/1081286514551501. URL http://mms.sagepub.com/content/early/2014/10/08/1081286514551501.abstract.

Siboni, M.H., Castañeda, P.P., 2014. Fiber-constrained, dielectric-elastomer composites: finite-strain response and stability analysis. J. Mech. Phys. Solids 68, 211–238. ISSN 0022–5096. http://dx.doi.org/10.1016/j.jmps.2014.03.008. URL http://www.sciencedirect.com/science/article/pii/S0022509614000489.

Singh, M., Pipkin, A.C., 1966. Controllable states of elastic dielectrics. Arch. Rational. Mech. Anal. 21, 169–210. ISSN 0003–9527.

Suo, Z., Zhao, X., Greene, W.H., 2008. A nonlinear field theory of deformable dielectrics. J. Mech. Phys. Solids 56 (2), 467–486.

Toupin, R.A., 1956. The elastic dielectric. Arch. Rational. Mech. Anal. 5, 849–915.

Vasseur, J.O., Deymier, P.A., Chenni, B., Djafari-Rouhani, B., Dobrzynski, L., Prevost, D., Apr. 2001. Experimental and theoretical evidence for the existence of absolute acoustic band gaps in two-dimensional solid phononic crystals. Phys. Rev. Lett. 86, 3012–3015. URL http://link.aps.org/doi/10.1103/PhysRevLett.86.3012.

Vasseur, J.O., Djafari-Rouhani, B., Dobrzynski, L., Kushwaha, M.S., Halevi, P., 1994. Complete acoustic band gaps in periodic fibre reinforced composite materials: the carbon/epoxy composite and some metallic systems. J. Phys. Condens. Matter 6 (42), 8759.

Wang, F., Lu, T., Wang, T.J., 2016. Nonlinear vibration of dielectric elastomer incorporating strain stiffening. Int. J. Solids Struct. 87, 70–80. ISSN 0020–7683. http://dx.doi.org/10.1016/j.ijsolstr.2016.02.030. URL http://www.sciencedirect.com/science/article/pii/S0020768316000925.

Wang, Y., Li, F., Kishimoto, K., Wang, Y., Huang, W., 2009. Wave band gaps in three-dimensional periodic piezoelectric structures. Mech. Res. Commun. 36 (4), 461–468. ISSN 0093–6413.

Wen, J., Wang, G., Yu, D., Zhao, H., Liu, Y., 2005. Theoretical and experimental investigation of flexural wave propagation in straight beams with periodic structures: application to a vibration isolation structure. J. Appl. Phys. 97 (11), 114907. http://dx.doi.org/10.1063/1.1922068. URL http://scitation.aip.org/content/aip/journal/jap/97/11/10.1063/1.1922068.

Zhao, X., Suo, Z., 2008. Electrostriction in elastic dielectrics undergoing large deformation. J. Appl. Phys. 104 (12), 123530. http://dx.doi.org/10.1063/1.3031483. URL http://scitation.aip.org/content/aip/journal/jap/104/12/10.1063/1.3031483.

Zhou, J., Jiang, L., Khayat, R.E., 2014. Electromechanical response and failure modes of a dielectric elastomer tube actuator with boundary constraints. Smart Mater. Struct. 23 (4), 045028.

Zhou, X., Chen, C., 2013. Tuning the locally resonant phononic band structures of two-dimensional periodic electroactive composites. Physica B 431 (0), 23–31.